An investigation of turbulent plane Couette flow at low Reynolds numbers

By KNUT H. BECH[1], NILS TILLMARK[2],
P. HENRIK ALFREDSSON[2] AND HELGE I. ANDERSSON[1]

[1]Faculty of Mechanical Engineering, The Norwegian Institute of Technology,
N-7034 Trondheim, Norway
[2] Department of Mechanics, Royal Institute of Technology,
S-100 44 Stockholm, Sweden

The turbulent structure in plane Couette flow at low Reynolds numbers is studied using data obtained both from numerical simulation and physical experiments. It is shown that the near-wall turbulence structure is quite similar to what has earlier been found in plane Poiseuille flow; however, there are also some large differences especially regarding Reynolds stress production. The commonly held view that the maximum in Reynolds stress close to the wall in Poiseuille and boundary layer flows is due to the turbulence-generating events must be modified as plane Couette flow does not exhibit such a maximum, although the near-wall coherent structures are quite similar. For two-dimensional mean flow, turbulence production occurs only for the streamwise fluctuations, and the present study shows the importance of the pressure–strain redistribution in connection with the near-wall coherent events.

1. Introduction

There seems to be a widespread consensus that wall-bounded turbulence is neither random nor deterministic, but that coherent and thereby deterministic structures can be identified, although their characteristics like location, size, spacing, strength and propagation velocity may vary within rather broad limits. Two of the most studied structures are the low-speed streaks in the viscous sublayer and the internal shear layer (ISL) which is mainly confined to the buffer region. There is a strong coupling between these structures: the shear layers are believed to be formed through lift-up of low-speed streaks from the viscous sublayer. This lift-up contributes to the Reynolds stresses in the near-wall region and thereby also to turbulence production. The shear layers are coupled to an instantaneous velocity profile with inflectional character and they have been observed to become unstable and break up into chaotic motion, so called 'bursting'. This phase is also believed to contribute to turbulence production and maybe the regeneration of the sublayer structure. The streaks and the ISL have also been suggested to be associated with streamwise vortices. The above description of near-wall turbulent structures may be sufficiently vague for almost everybody to agree upon; when it comes to details there is much less agreement. This is so not only on the structural aspects, but also on time scales, Reynolds number dependence, etc. To some extent this depends on the fact that there is no obvious way to extract information on the randomly appearing coherent structures from experimental and/or numerical data and many times researchers have developed their own methods which

has made comparisons between various studies difficult. Most of the research has been carried out in plane channel flows and zero pressure gradient boundary layers; very few studies have been made in non-zero pressure gradient boundary layer flows or pipe flows and none so far in plane Couette flow.

The first studies of coherent structures were made by means of flow visualization; notable are the experiments carried out at Stanford University (Kline *et al.* 1967 and Kim, Kline & Reynolds 1971). To capture the structures observed in the experiments in pointwise measurements conditional sampling techniques for data evaluation were developed. To detect when a structure is at hand some criterion has to be fulfilled. In the near-wall region a fixed observer will see a high value of the temporal derivative of the streamwise velocity when the ISL passes by. This feature of the bursting sequence is utilized in the so-called VITA (Variable Interval Time Averaging) technique which has been used in several experimental investigations (see e.g. Blackwelder & Kaplan 1976 and Johansson & Alfredsson 1982) to detect shear-layer structures in boundary layers and channel flows. Although this method detects a feature of the streamwise velocity signal at one position it has been shown to detect structures which are strongly coupled to turbulence production.

The development of simulation methods for turbulent flows has revolutionized the work carried out on detecting the turbulence-producing events. Many quantities that are extremely hard to measure in the laboratory can in principle be easily determined when the data bases obtained from simulations are at hand. The numerical simulations have confirmed the experimental observations that a large portion of the turbulence production is strongly intermittent both in time and space (Johansson, Alfredsson & Kim 1991, in the following referred to as JAK). In plane Poiseuille flow large contributions to the Reynolds stress have mainly been found directly associated with the lift-up of low-speed fluid, i.e. on the downstream side of the internal shear layers in the buffer region. Thus the formation and evolution of shear-layer-like structures in the near-wall region of turbulent flows have been recognized to be intimately coupled to turbulence production.

In the present study coherent structures in the near-wall region of plane Couette flow are studied with the use of both numerical simulations and physical experiments and comparisons with, in particular, plane channel flow are made. Many similarities but also differences are found which may help in determining the role of coherent structures in the turbulence-generating process.

1.1. *Turbulent Couette flow*

Turbulent plane Couette flow is one of the canonical flow cases and among its interesting and distinguishing features (as compared to pressure-driven flows such as plane channel flow) are the monotonic velocity profile (see figure 1), the constant shear stress distribution †

$$-\overline{uv} + \frac{\mathrm{d}U}{\mathrm{d}y} = 1 \tag{1.1}$$

and, at all positions across the channel, the finite turbulence production rate $\mathscr{P}$

---

† In the following all quantities are normalized with the viscous scales, i.e. friction velocity $u_\tau = (\tau_w/\rho)^{1/2}$, viscous length $l_* = \nu/u_\tau$ and viscous time $t_* = \nu/u_\tau^2$, $Re_\tau = u_\tau h/\nu$. U is the mean (streamwise) velocity and u, v, w the fluctuating components in the streamwise (x), wall-normal (y) and spanwise (z) directions.
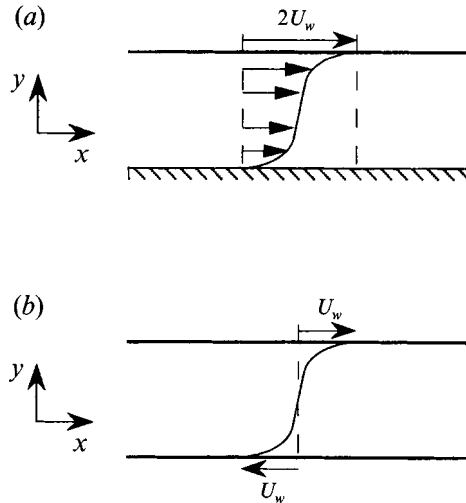
FIGURE 1. Mean velocity distribution in turbulent plane Couette flow: (*a*) one stationary and one moving wall, (*b*) two walls moving in opposite directions.

$$\mathscr{P}(y) = -\overline{uv}\frac{\mathrm{d}U}{\mathrm{d}y}$$

of turbulent kinetic energy $k = \frac{1}{2}(\overline{u^2} + \overline{v^2} + \overline{w^2})$ †. For plane Couette flow the transitional Reynolds number, i.e. the Reynolds number $Re = U_w h/v$ for which turbulent spots will survive, is approximately 360 (based on half channel height, h, and half the velocity difference between the walls, U_w), whereas fully developed turbulence is obtained at Reynolds numbers above approximately 500.

Although a few studies (both experimental and numerical) have been aimed at determining the mean flow and Reynolds stress distributions in this flow almost nothing is known about the near-wall coherent structures which in other wall-bounded flows are the main contributors to turbulence production. It seems plausible that coherent structures in the near-wall region are similar in various wall-bounded flows; however there may be special features depending on the flow in question. It is natural to scale wall events with the viscous scales; however the time and length scales of events may involve the Reynolds number to a certain power. For instance it has been suggested that the occurrence and time scale of turbulence-generating events scaled with the viscous scales vary as the square root of the Reynolds number (so-called mixed scaling, see Alfredsson & Johansson 1984). These Reynolds number trends may be different in various flows. For instance in plane Couette flow the turbulence production is finite across the channel which may result in a stronger interaction between the outer and inner regions as compared to channel flow.

In channel and boundary layer flows the Reynolds stress as well as the turbulence production have maxima close to the wall and then decrease towards zero at the channel centreline or in the free stream. The maxima close to the wall are usually associated with the near-wall turbulence-producing coherent structures. In plane Couette flow, however, the Reynolds stress increases monotonically from the wall to

† In fact for plane flows the production is only in the streamwise fluctuating component. Transfer to the other components is through pressure–strain redistribution.

an (almost) constant level in the core region, whereas the turbulence production still has a maximum close to the wall.

1.2. *Previous experimental and numerical Couette flow studies*

Many different approaches have been taken to experimentally establish plane Couette flow. From the fluid dynamic point of view the easiest way is to use an apparatus with counter-moving walls. In this way the fully developed state is only dependent on the diffusion of vorticity from the walls across the channel and the length of inlet regions at both ends of the channel is probably only a few channel widths. In this case the net transport of fluid along the channel is zero. Measurement probes inserted in such a set-up will give rise to disturbances that propagate in both directions which will make such measurements unfeasible. However, it is ideally suited for non-intrusive measurement methods, such as flow visualization or LDV. For hot-wire anemometry it is necessary, both from the disturbance point of view but also because a well-defined mean velocity direction is needed, to use one stationary and one moving wall. In this case the correct volume flux is not possible to achieve with the moving wall alone; in addition a pressure gradient has to be established along the inlet part of the channel which should be matched to the wall speed to give the required flux through the channel. Ideally one could think of a top-hat velocity profile (with velocity U_w) at the inlet which will be modified due to viscous stresses at the two walls. This will give rise to a transport of fluid from the side of the stationary wall towards the moving one before the velocity profile is established.

The first experiment on plane Couette flow was carried out by Reichardt (1956) in a running belt apparatus with both walls moving. He used oil and water as fluids and reported measurements of the mean velocity profile. Reichardt (1959) also made measurements in an air channel with one moving wall and reported mean velocity measurements for turbulent flow at $Re = 17\,000$. Robertson (1959) and later Robertson & Johnson (1970) made measurements in air with pitot tubes and hot-wire anemometry in an apparatus with one stationary and one moving wall. In that apparatus air was supplied to the inlet with a fan to obtain the correct mass flux in the channel. Aydin & Leutheusser (1979, 1987, 1991) used a moving plate suspended above a straight plate (32 m long) and carried out hot-wire measurements to obtain the mean and r.m.s. of the streamwise velocity. In this case they had an entrance with a contraction acting as a funnel and a screen combination to establish a suitable entrance flow. Finally El Telbany & Reynolds (1982) used a moving belt and one rigid wall together with an inlet blower to establish the flow.

An apparatus designed by us (Tillmark & Alfredsson 1991, 1992), which uses an 'infinite' plastic band moving along vertical glass surfaces in water, was originally constructed for studies of transition in plane Couette flow. By using a transparent plastic band it is possible to use Laser-Doppler velocimetry (LDV) (or flow visualization) for non-intrusive measurements. This apparatus has also been used by Tillmark & Alfredsson (1993, 1994) for measurements on one-point long time statistics of the streamwise velocity (mean velocity, r.m.s., skewness and flatness), as well as two-point space–time correlations. Measurements were made for Reynolds numbers between 1200 and 3500. Measurement techniques included both LDV and hot-film anemometry.

A list of different direct numerical simulations of turbulent Couette flow is given in table 1, together with details of the computations. The numerical simulation by Lee & Kim (1991) has shown persistent counter-rotating streamwise vortices of extremely long length scale giving rise to high- and low-speed streaks in the central region of the

flow. These structures were associated with 30% of the total turbulent energy. Direct numerical simulations by Kristoffersen, Bech & Andersson (1993) show similar but much weaker structures. It seems probable that the simulation made by Lee & Kim (1991) suffered from using too small a box length (it was approximately $12h$) and that they thus obtained a continuous forcing of elongated structures. The spanwise size of the box (approximately $8h$) may have restricted the spanwise movement of the vortices and made them more persistent than in an experiment with a large aspect ratio. However it is also clear from the measurements of Tillmark & Alfredsson (1994) that there exist large-scale structures in turbulent plane Couette flow that do not have a counterpart in for instance plane Poiseuille flow and that this will lead to great difficulties in trying to simulate this flow numerically or experimentally. Such structures may be inherent in this flow since Nagata (1990) and Clever & Busse (1992) both have shown that solutions involving large-scale streamwise vortices can also exist in laminar plane Couette flow.

The present paper describes new experimental and numerical data on turbulent Couette flow at *Re* of about 1300. These data are used to analyse the role of coherent structures in the near-wall region. The numerical simulation code and the data base will be described in §2, and the relevant details of the experimental apparatus and measurement techniques are given in §3. Comparisons between long time statistics from the measurements and the numerical simulations are made in §4 and results regarding the near-wall structures are given in §5, where both comparisons between experimental and numerical results are given and also comparisons with similar investigations in channel flow. Finally the results are discussed in §6 where similarities and non-similarities between Couette flow and plane Poiseuille flow are discussed.

2. Numerical simulation of turbulent Couette flow

2.1. *The computer code*

The present direct numerical simulation (DNS) was carried out utilizing a finite-difference computer code originally developed by Gavrilakis *et al.* (1986). In this code the incompressible momentum equations are discretized by the second-order-accurate central-difference scheme. The Poisson equation for the pressure is Fourier-transformed with respect to the streamwise and spanwise homogeneous directions and the resulting three-diagonal equations are solved directly for each time step. The flow field is advanced in time using a fractional-step method and with the second-order Adams–Bashforth time discretization scheme. At the walls, no-slip boundary conditions are imposed on the velocity components. Periodicity is assumed in the streamwise and spanwise directions. The computational mesh is homogeneous except for the wall-normal direction. Kristoffersen & Andersson (1993) applied the code with minor modifications to perform DNS of turbulent channel flow with spanwise rotation. Results for the non-rotating case were published by Andersson & Kristoffersen (1992).

2.2. *The present computation*

The case-specific information of the present computation is listed in table 1. The effect of the streamwise and spanwise geometrical length scales L_x and L_z on numerically generated turbulent Couette flow was investigated through a series of large-eddy simulations (LES) with different computational boxes at the present Reynolds number. These simulations were performed using the sub-grid model due to Moin & Kim (1982). The LES indicated that by choosing $L_z/h = 4\pi$, the turbulent field was

Case	Sampling time	Re_τ	$N_1 \times N_2 \times N_3$	L_x/h	L_z/h	Δx	Δz	Δy (min, max)
Present	1350	82.2	$256 \times 70 \times 256$	10π	4π	10.1	4.0	(0.7, 3.9)
Kristoffersen et al. (1993)	1740	83.2	$96 \times 64 \times 64$	4π	2π	10.9	8.2	(0.2, 6.4)
Lee & Kim (1991)		170	$192 \times 129 \times 288$	4π	$8/3\pi$	11.1	4.9	
Papavassiliou & Hanratty (1994)	2250	150	$128 \times 65 \times 128$	4π	2π	14.8	7.4	
Miyake et al. (1987)		62	$64 \times 32 \times 64$	64	16	61.6	15.4	

TABLE 1. Direct numerical simulations of Couette flow (all variables in viscous units). L_x and L_z are the dimensions of the computational box in the streamwise and spanwise directions, while Δx etc. denotes the grid spacing.

allowed to decorrelate in the spanwise direction. In addition, these simulations suggested that the 'infinite', large-scale eddies observed by Lee & Kim (1991) were one of (at least) two possible states of the large-scale turbulent field in Couette flow. Another, more disordered state with less turbulent kinetic energy and smaller eddies was the most common in the LES and was similar to the statistically steady solution of the present computation. In order to match the box size of the present computation to both these flow states, $L_z/h = 4\pi$ was considered to be a good choice. The aspect ratio was close to an even, integer number (6), leaving room for three pairs of counter-rotating vortices similar to those observed by Lee & Kim. In addition, the relatively large aspect ratio made the disordered state possible.

The computational domain should capture at least two 'average' near-wall low-speed streaks and the ratio L_x/h should be relatively large in Couette flow DNS because of the possible existence of elongated structures in the core region. The length of the computational box was chosen as $L_x/h = 10\pi$, which is approximately 2600 wall units at the present Reynolds number. This was found to be a reasonable compromise between the two conflicting goals of a large streamwise box length and a good streamwise resolution. A study of the influence of L_x and L_z on the one- and two-point correlations of u in three different DNS of the present flow case was carried out by Bech & Andersson (1994). The use of a computational box with a long streamwise extent and a small aspect ratio was found to trigger eddies of very large streamwise extent. The results of the present computation were found to be very similar to those of Kristoffersen et al. (1993) concerning the streamwise one-point correlation and the spanwise two-point correlation. The elongated streamwise structures and the small-scale resolution were, however, better simulated in the present computation.

In table 1 it is seen that the box length, in terms of channel heights, is 2.5 times larger in the present case compared to Lee & Kim (1991) and Papavassiliou & Hanratty (1994). By choosing a low Re, the dimensions of the computational box could be relatively large without having to use too coarse a computational mesh.

The initial field for the present DNS was generated by interpolating a LES flow field from a $64 \times 32 \times 64$ grid to a $256 \times 70 \times 256$ grid. The LES flow field had been run for 3500 t_*. The DNS was then run for 1300 t_*, before the sampling process was started. During the first 400 of these 1300 time units, a transient behaviour occurred

during which the volume-averaged turbulent kinetic energy k decreased. (The too high initial level of k was caused by the crude resolution and the sub-grid model in the LES.) During the remainder of the 1300 time units, the planar averages of the turbulence quantities were fluctuating about approximately statistically steady mean values. Because the expected large-scale vortical cells with a high degree of spanwise periodicity were not present in the flow field, the time advancement was considerable before starting the sampling in order to ensure that the large-scale field really was statistically steady. The flow field did not enter into the state with substantial periodicity during the run.

In order to satisfy (1.1) and to get sufficiently smooth time-averaged two-point correlations for calculating the one-dimensional energy spectra, the calculation was run for another 1300 t_* during which a data-base of flow fields was generated and time-averaged statistics were calculated. The data-base consisted of 12 fields of the primitive variables u, v, w and p recorded with 12 t_*-intervals. During the computation, the Courant number was kept below 0.3, the definition of the CFL-condition being the same as in Gavrilakis (1992). The computation was performed with a time step of 0.03. The maximum fluctuation of the volume-averaged kinetic energy during sampling was below 10% of the mean value. The computation was run on a Cray Y-MP using 1 CPU and 344 Mb of memory. The cost per time step was 6.4 CPU-seconds. The post-processing of the data base was run on a DEC DS 5240 computer. The marginal computer memory available restricted the conditional sampling presented in §5 to one half-channel, i.e. only flow fields contained between the centreplane and one of the walls were considered.

2.3. *Numerical resolution*

One-dimensional spectra will not provide definite information regarding the resolution of the smallest turbulence scales in a finite-difference DNS like they do in spectral-method DNS. However, experience shows that too poor a resolution corrupts the spectra. The spectra give an impression of the range of length scales present in the simulation. The decay rate at high wavenumbers provides information regarding the amount of energy associated with the smallest length scales. Figure 2 displays spectra at two different y-values: one in the viscous sub-layer and the other corresponding to the centreplane.

For the streamwise spectra in figure 2(a), the energy decays at least 6 decades. For intermediate streamwise wavenumbers, the spectra contained more energy than found by Kim, Moin & Moser (1987) in Poiseuille flow. The pile up of energy around $k_x h = 10$ caused the spectra to drop sharply at high wavenumbers. The spanwise spectra are also monotonically decreasing in the high-wavenumber range. E_{vv} displays the shortest span in energy, especially near the wall where the drop is slightly more than 3 decades. The amount of energy contained in the small-scale wall-normal motions close to the wall was, however, considered to be relatively small.

Because the spectra indicated that the wall-normal velocity was most likely to be inadequately resolved very close to the wall, some further studies concerning the numerical resolution of this velocity component were carried out by studying the higher-order moments in the immediate vicinity of the wall. The results of a comparison of these quantities with DNS data published by various authors are presented in Bech & Andersson (1994). Figure 6(a) in §4.1 shows that the derivative of the skewness factor $S(v)$ changes sign at $y = 14$. This behaviour was similar to that observed by Kim *et al.* (1987) and Gavrilakis (1992). Closer to the wall, however, the skewness of v remained negative, while $S(v)$ became positive in the DNS by Kim
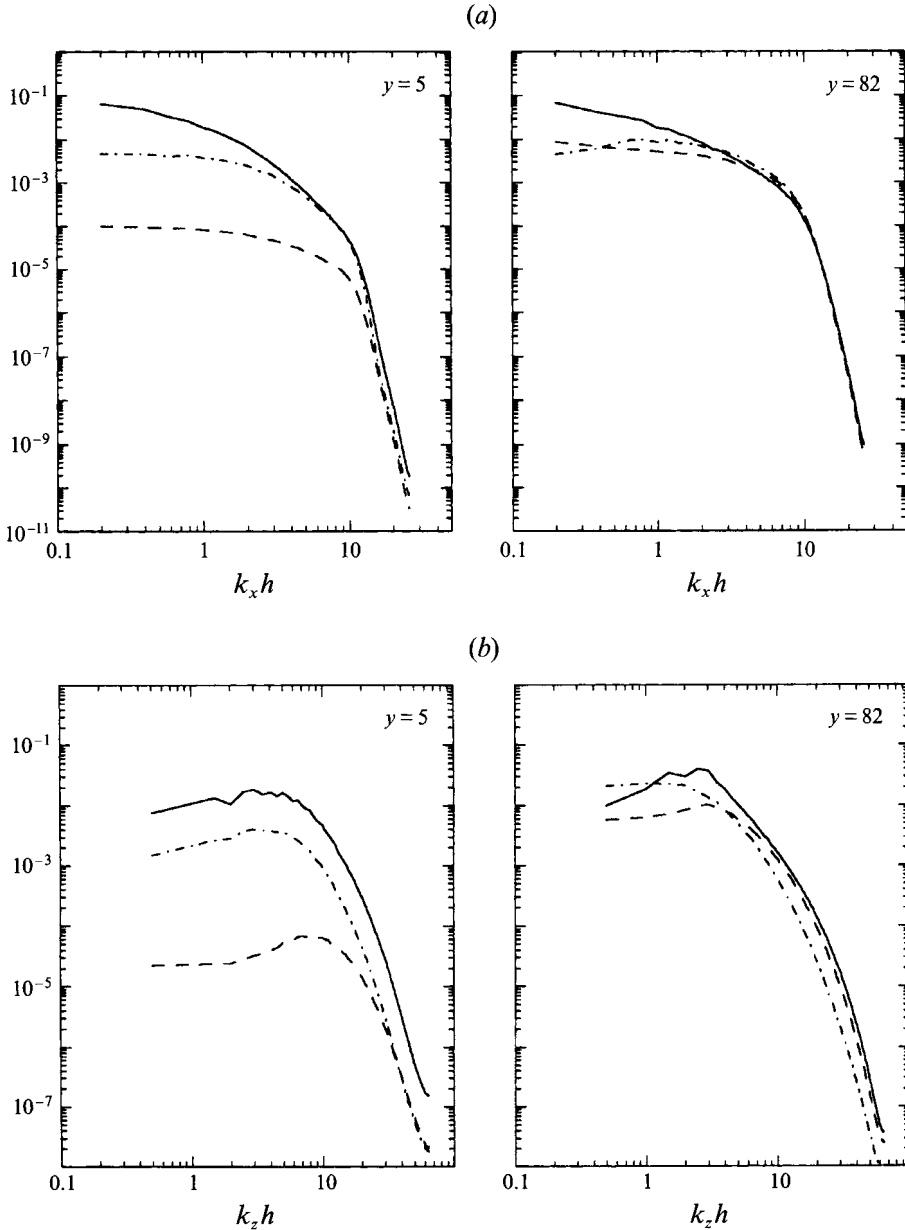
(a)

(b)

FIGURE 2. One-dimensional energy spectra as functions of streamwise wavenumbers (a) and spanwise wavenumbers (b) from numerical simulation of turbulent Couette flow. —, E_{uu}; - - -, E_{vv}; - - -, E_{ww}.

et al. (1987). It should be recalled that $S(v)$ is more difficult to obtain than $S(u)$ and $S(w)$ as demonstrated by Andersson & Kristoffersen (1992). In the same figure, the skewness factor $S(w)$ is observed to diverge from zero, i.e. the theoretical value due to symmetry, when the wall is approached. The value was 0.04 at the wall. This may be a result of a marginal number of grid points between the wall and $y = 2$.

The problem of numerical resolution in the case of Couette flow DNS is associated with the largest scales. The two-point correlations in figure 8 (§4.2) indicate that

the turbulent velocity fluctuations decorrelated at separations corresponding to half the computational box with some exceptions: $R_{uu}(L_x/2h)$ was approximately 0.01 at $y = 13$ and 0.03 in the channel centre, this being the absolute maximum of the correlation at this separation. A weak periodicity in $R_{uu}(\Delta z)$ resulted in a 2% maximum correlation in the centreplane for $\Delta z = L_z/2$. These minor shortcomings of R_{uu}, which ideally should decay to zero at separations corresponding to the half-box size, may be caused by the finite computational box. However, the deviations from zero correlation were relatively small when compared to other DNS of turbulent Couette flow (Bech & Andersson 1994) and the present DNS was considered as the most consistent and reliable available.

3. Experimental apparatus, measurement procedure and data processing

3.1. *Experimental apparatus*

The experiments were carried out in the plane Couette flow apparatus previously described by Tillmark & Alfredsson (1992).

The apparatus is of infinite belt type and water is used as the working medium. The main part of the rig is an open, more or less rectangular shaped container 400 mm high with one of the longer vertical walls (400 mm × 1500 mm) made of float glass. To form the plane Couette channel a glass plate of the same size is placed inside the tank, parallel to and at a short distance from the glass wall. Depending on the mode of operation the 360 mm wide transparent belt slides along one or both facing glass surfaces of the channel. The belt is made of a 5 m long polyester film (type 'overhead film') with the ends glued together in a thin joint and is driven by a rotating cylinder in each end of the tank. The distance between the belt and the bottom of the tank is 20 mm and the top of the channel has a free fluid surface. A microscope is used to determine the channel height as well as to check the belt position continuously.

A special feature of the apparatus used in the present study is that two counter-moving walls may be used (figure 3a). However it can also be run in a single wall configuration (figure 3b). In that case half of the belt loop runs outside the channel and the main flow is unidirectional making it accessible to measurements with probes inserted into the flow from a downstream position. To obtain the correct mass flux through the channel a pressure difference between the inlet and outlet of the channel in addition to the moving wall is required. This is achieved by pumping water from the outlet to the inlet. The level of the free water surface shows that the pressure drop is concentrated in short entrance region about $20h$ long.

3.2. *Hot-film measurements*

To be able to use hot-film probes the Couette channel was run in single moving wall mode. The channel width was set to 20 mm leading to an aspect ratio of 18. A vertical tripping rod was placed in the channel inlet to reduce the length of the turbulence transition region.

Aydin & Leutheusser (1979) experimentally investigated the necessary entrance length needed to acquire fully turbulent Couette flow and found that for locations more than $100h$ downstream of the inlet the measured velocity profiles were identical. In our case all measurements were carried out halfway between the bottom and the free water surface at a location $138h$ downstream of the inlet to ensure fully developed turbulent flow.
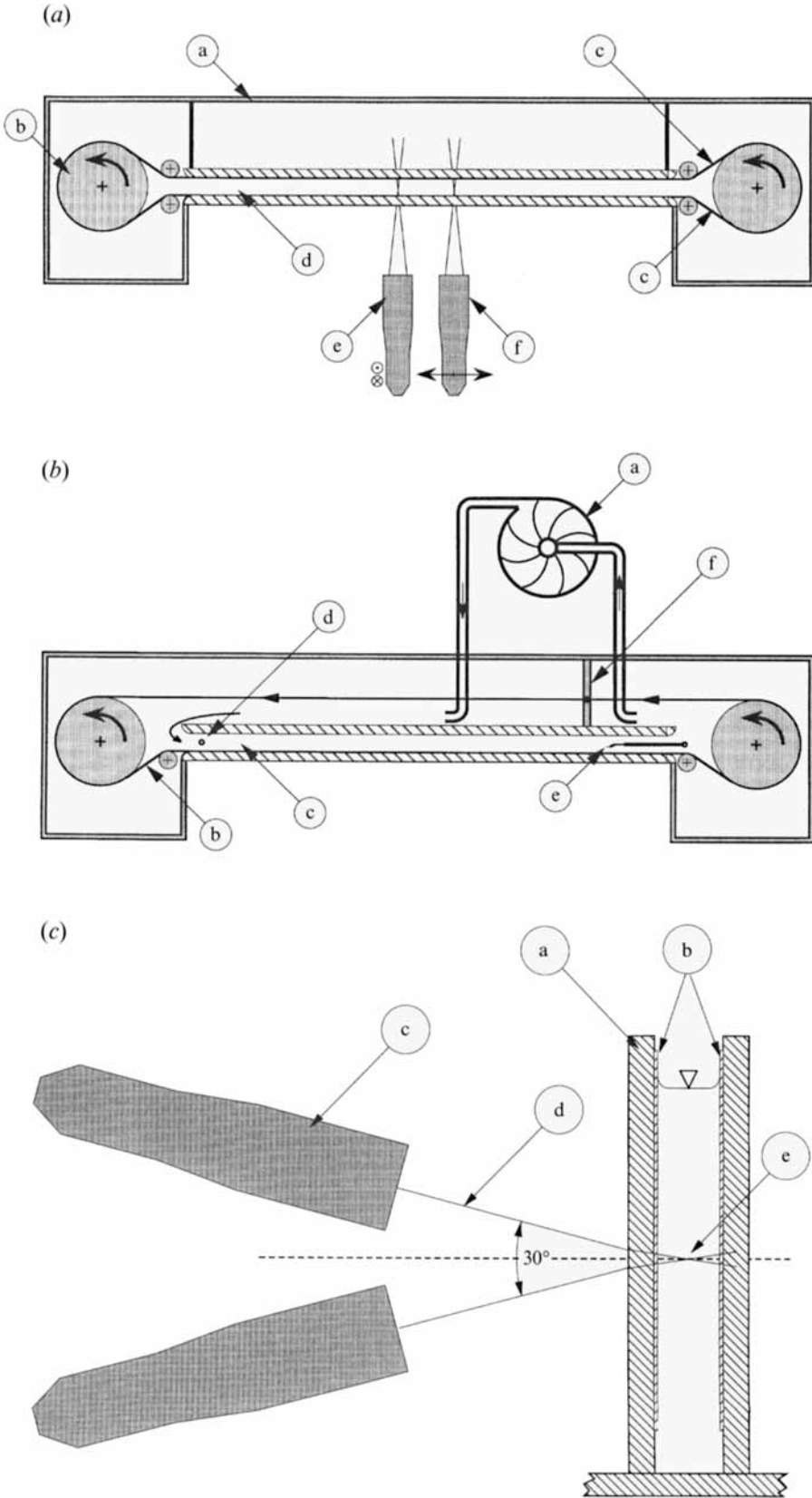
(a)

(b)

(c)

FIGURE 3 (*a–c*). For caption see facing page.

A DISA 55M01 anemometer system and boundary layer type sensors (DANTEC R15) 1.25 mm long, 70 μm in diameter were used to obtain the streamwise velocity component. The sensor length was 10 l_* in the experiment, which ensured good spatial resolution, as shown by Johansson & Alfredsson (1983).

The probes were calibrated in a submerged water jet in a separate tank and the hot-film signal was collected through a 12 bit A/D converter (Microlink) and stored on a harddisk in an IBM AT compatible computer. The calibration curve consisted of two parts thereby keeping the maximum velocity error to less than 2% over the entire range. For both velocity ranges an expression of the form

$$U = k_1(E^2 - E_0^2)^{1/n} + k_2(E - E_0)^{1/2}$$

was used, where E is the anemometer output voltage at velocity U. E_0 is the anemometer output at zero velocity and k_1, k_2 and n are constants adjusted for best fit of the equation to the calibration data in the velocity interval.

The probes were run at 16°C overheat temperature and the water in the tank was held at constant temperature within ±0.02°C. The output signal was collected and stored by the same equipment as was used in the calibration routine for later evaluation on an IBM workstation RS6000. For the mean velocity profile and the higher central moments, sampling rate was 250 Hz. Velocity data were acquired only during the period when the belt joint was outside the channel. Sixty such records of 1750 samples were taken at each spatial position. In the correlation measurements the sampling rate was increased to 500 Hz and 100 records of 4096 samples were taken.

The streamwise velocity component was obtained in two different sets of measurements: single probe measurements where the probe was traversed in the cross-flow direction at $Re = 1260$ and measurements with one fixed and one movable probe to acquire the spanwise correlation function at $Re = 1500$.

In the single probe measurements a traversing mechanism with a resolution of 10 μm was used to move the probe from the stationary wall towards the moving wall covering the span $0 < y/h < 1.40$. Its position relative to the wall was determined using a microscope. In the correlation measurements two probes were located halfway between the vertical walls at the same downstream position. One probe was held at a fixed position and the other was traversed vertically and parallel to the walls towards the free water surface. The probe supports and the traversing system limited the separation distance of the two sensors to be between 4.5 mm and 43 mm, equivalent to $0.44 < z/h < 4.23$.

3.3. *LDV measurements*

Two-point LDV measurements of the fluctuating streamwise velocity were made to determine the spatial correlations with either streamwise or spanwise separation. Approximately the same Reynolds number was used as in the hot-film measurements. The Couette channel was operated with both walls moving and the channel height

---

FIGURE 3. Top view of experimental apparatus. (a) Configuration with two moving walls. a: outer compartment, b: driving cylinder, c: plastic belt formed into an infinite loop, d: plane Couette channel, e: laser probe head (movable in vertical direction), f: laser probe head (movable in horizontal direction). (b) Configuration with one moving and one stationary wall. a: pump, b: plastic belt, c: plane Couette channel, d: tripping rod, e: hot-film probe, f: barrier, separating inlet from outlet. (c) Close up view of laser heads arrangement. a: Couette channel glass walls, b: plastic belt, c: probe head, d: plane of the laser beams, e: probe volume.

was changed to 10 mm and by that the aspect ratio was increased to 36. In this case the viscous scales were $t_* = 3$ ms and $l_* = 0.06$ mm.

The measurements were carried out with an Aerometrics LDV system consisting of a 5W Ar^+ laser, two fibre-optic probe heads working in backscatter mode and a frequency domain signal processor DSA3000. To avoid direction ambiguity one of the beams in each probe head was frequency shifted. The signal processor was controlled by a Victor V486M/33 PC-computer, which also handled and analysed the data on line.

The probe heads were placed on separate machine tables on the same side of the Couette channel bringing the main axis of the probe volumes in the crossflow direction (see figure 3c). The heads could be moved with high precision in three perpendicular directions. The position of the measuring volume relative to the glass walls during spanwise or streamwise traversing varied by less than 1% of the channel height. A lens with a focal length of 300 mm was used as a front lens in the probe heads and the length and diameter of the ellipsoidal measuring volume was 0.9 mm (corresponding to 15 l_*) and 0.09 mm respectively. Owing to spatial restrictions, the optical axis of the probe heads had to be inclined $\pm15°$ in the vertical-normal plane of the glass surfaces making full overlap of the probe volumes impossible and hence reducing the obtainable correlation coefficient below its theoretical value of 1 at this point. Data collection was blocked electronically when the belt joint was between or closer than $10h$ to the measuring volumes.

To minimize grinding damages on the glass surfaces and the belt, non-abrasive seeding particles had to be used in the flow and several tests were carried out with plastic particles of different sizes to optimize the signal-to-noise ratio. A main noise source was found to be the diffusely scattered background light due to the micro scratches in the plastic belt. The best result was obtained using unexpanded KemaNobel Microspheres with a mean diameter of slightly less than 10 µm.

The correlation measurements were made in the central plane $y = h$ of the channel at $Re = 1300$. To minimize the amount of data that had to be saved, the processor was run in coincidence mode. 3000 data points were collected at each spatial position. It was found that increasing the number of data points drastically at this level only marginally changed the correlation coefficient. Each accepted data point had a dual channel time overlap of at least 10% of the Doppler burst lengths. This scheme in addition to the demand for high signal-to-noise ratio gave a mean data rate of 2 to 4 points per second, which means that individual data points were separated by the order of the integral time scale. To further minimize false data, single data pairs where the velocity exceeded the mean velocity by 3.5 times the r.m.s. value were excluded. This extra filter function only ruled out 1% of the data but substantially refined the correlation coefficient.

The two-point spatial correlation coefficients of u, $(R_{uu}(\Delta x_i))$, in both streamwise and spanwise directions were determined using the estimator given by

$$R_{uu}(\Delta x_i) = \frac{1}{N} \sum_{j=1}^{N} \frac{u_j(x_i)u_j(x_i + \Delta x_i)}{u_{rms}(x_i)u_{rms}(x_i + \Delta x_i)}$$

where N was the number of samples (3000 in this case). The local mean velocity was based on the 3000 samples and found to be very close to zero at all measuring points. In the data processing to obtain the correlation function no (residence time) weighting of the individual velocity data was applied.
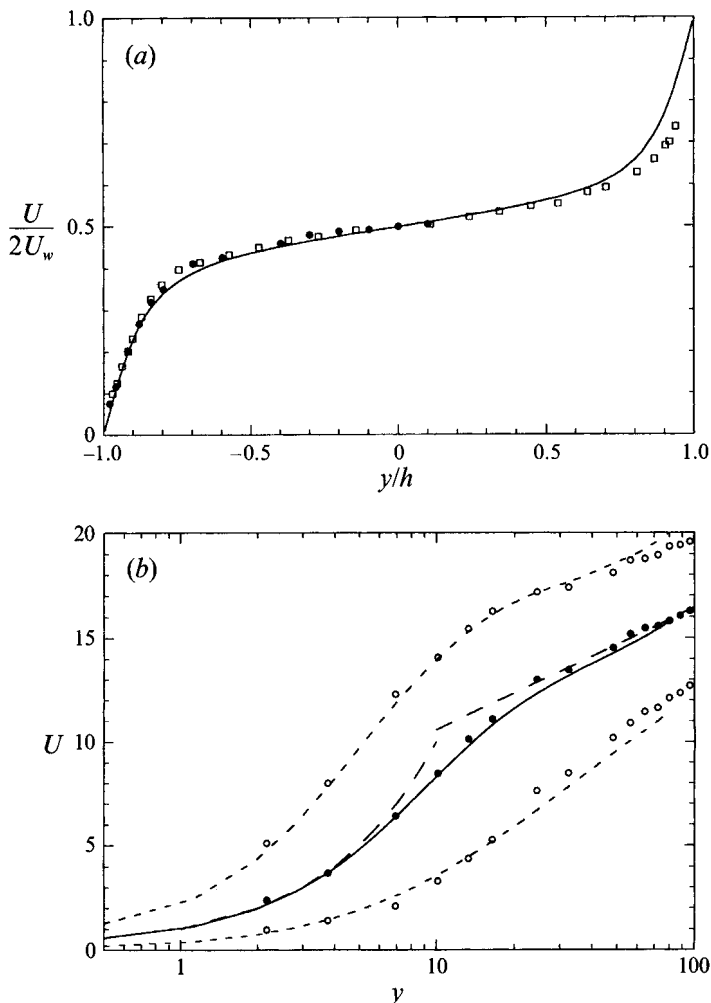
FIGURE 4. (*a*) Velocity distribution: •, present experiment, $Re = 1260$; —, present DNS, $Re = 1300$; □, Aydin & Leutheusser (1987), $Re = 1300$. Note the translation of $y = 0$ compared to the other figures. (*b*) Velocity distributions with viscous normalization: •, present experiment, $Re = 1260$; —, present DNS, $Re = 1300$. Also shown are the 98% limits of the probability density distribution: ○, experiment; - - -, DNS. — — —, $U = y$ and $U = 2.55 \ln y + 4.7$.

4. Long time statistics

4.1. *Mean velocity, r.m.s. and higher central moments*

The long time statistics were obtained from direct numerical simulation and hot-film measurements at Reynolds number equal to 1300 and 1260, respectively. The hot-film measurements were made with one moving and one stationary wall and all measurements were taken in the part of the channel adjacent to the stationary wall. In order to be able to make accurate comparisons between these two data sets, as well as with other data, it was important to determine the wall friction velocity correctly. Too few measuring points were available in the viscous sublayer in the experiment to determine the wall shear stress with the high precision needed, so instead the $Re_{\tau,exp}$ (the experimental Reynolds number based on wall friction velocity) was determined
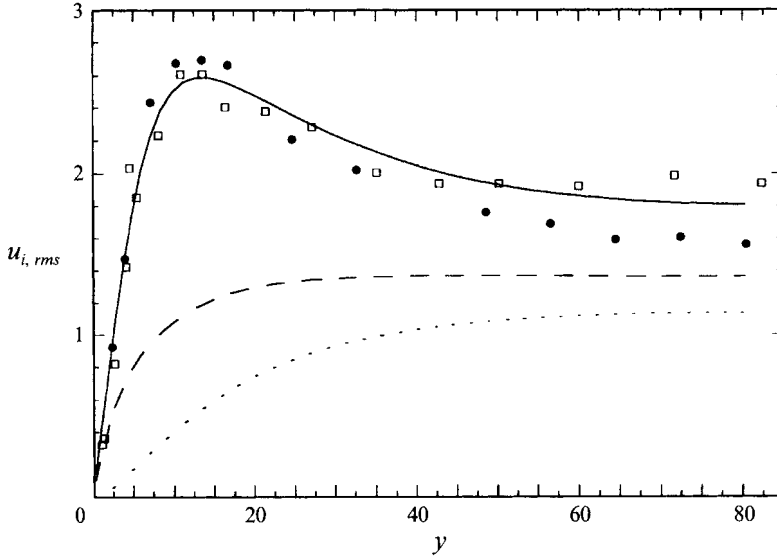
FIGURE 5. Distribution of the root-mean-square values of the fluctuating velocities from DNS: —, u_{rms}; $\cdots$, v_{rms}; — — —, w_{rms} and experiments: ●, u_{rms} present experiment, $Re = 1260$; □, u_{rms} Aydin & Leutheusser (1991), $Re = 1352$.

using the relation

$$Re_{\tau,exp} = Re_{\tau,DNS} \frac{Re_{exp}}{Re_{DNS}}.$$

With $Re_{\tau,DNS} = 82.2$ in the simulation the experimental $Re_{\tau,exp}$ was determined to 79.7. Obtaining the friction velocity in this way the experimental values of the viscous scales were $t_* = 12$ ms and $l_* = 0.11$ mm.

The mean velocity distribution from the experiment and the simulation are shown in figure 4(a,b). For comparison experimental values obtained by Aydin & Leutheusser (1987) at $Re = 1300$ are also plotted in figure 4(a) and the data points from the two experiments align well. Close to the wall there is an excellent agreement between the simulation (the full line) and the experimental points, but in the centre of the channel the experimentally determined velocity gradient is less steep than the gradient obtained from the simulation.

The mean velocity in figure 4(b) is plotted in a semi-logarithmic form, normalized with viscous scales. As expected, the velocity profile can be divided into a viscous sublayer, a buffer region and a logarithmic part, but no wake region can be distinguished, probably due to the low Reynolds number. It is evident from figure 4(b) that to be able to experimentally determine a correct velocity gradient at the wall from an estimate based on the measurement points, only points below $y = 4$ should be used. In addition to the DNS and experimental data, the familiar logarithmic relation

$$u = A \ln y + B$$

with the constants adapted to the experimental points is drawn in figure 4(b) for comparison. Only small deviations from the straight line are found in the outer region up to the central plane. A value of 2.55 for the constant A from both experiments and simulation agrees with what has been found by others in plane Couette flow (El Telbany & Reynolds 1982; Aydin & Leutheusser 1991) but the
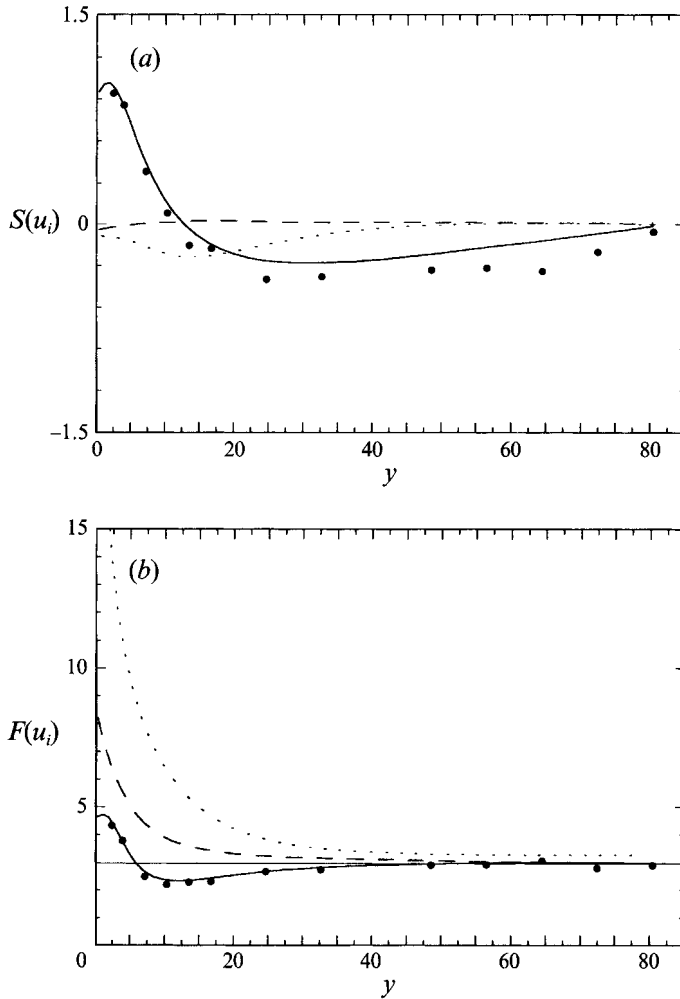
FIGURE 6. Distribution of higher statistical moments. (a) Skewness. DNS: —, $S(u)$; $\cdots$, $S(v)$; - - -, $S(w)$. Experiments: •, $S(u)$, (b) Flatness. DNS: —, $F(u)$; $\cdots$, $F(v)$; - - -, $F(w)$. Experiments: •, $F(u)$.

additive constant B is 4.7 and 4.5 for the experiment and simulation respectively, which is slightly lower than previously reported values.

To get a general view of the local streamwise fluctuations the 98% span of the velocity probability function is also shown in figure 4(b). The span is fairly symmetric around the mean velocity in the central part of the channel and increases its width in the buffer region. The largest span is found around $y = 12$ and also at this position the streamwise turbulence intensity (figure 5) reaches its maximum. Closer to the wall the span decreases and the distribution becomes unsymmetrical due to the solid wall boundary conditions. In figure 5 turbulence intensities from DNS and experiments are shown. The highest intensity is found in the streamwise component which has a distinct maximum around $y = 12$ whereas the other components monotonically increase to a constant value in the centre of the channel. At the centreline the ratio between the normal and streamwise fluctuations is about 2/3. This ratio is about the same as in turbulent channel flow despite the differences in the v_{rms} and w_{rms}
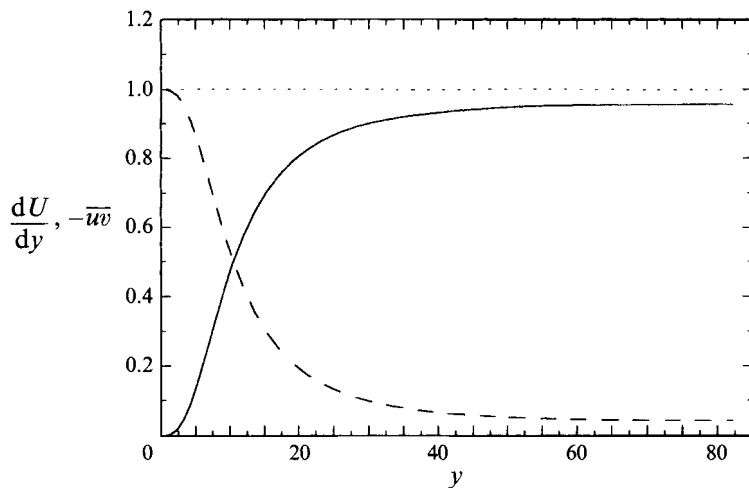
FIGURE 7. Distribution of shear stress across the channel obtained from simulation:
— —, $\overline{uv}$; - - -, $\mathrm{d}U/\mathrm{d}y$; $\cdots$, $\mathrm{d}U/\mathrm{d}y - \overline{uv}$.

distributions which for the channel flow have maxima near the wall and minima at the centre of the channel. However the absolute levels for Couette flow in the central plane are twice as high. Figure 5 also shows that the simulation and experimental data compare very well quantitatively in the near-wall region up to $y = 8$ but in the buffer region the experimental values are around 8% higher than the intensity obtained from the DNS. Beyond this region the experimental data points decrease more rapidly giving a 15% lower turbulence intensity in the centre as compared to the simulation. The experimental data by Aydin & Leutheusser (1991), were obtained at almost the same Re ($= 1352$). These data † show good overall agreement with the DNS data but have an almost constant level in the central region in contrast to the decreasing DNS values. The large difference (about 20%) in turbulence intensity in the outer region of the flow between the present experiment and that of Aydin & Leutheusser (1991) can probably not be explained by experimental scatter but must be sought in differences of the experimental apparatuses.

The third (skewness) and fourth (flatness) central moments are presented in figure 6(*a*, *b*) and show reasonable agreement between simulation and experiment. The location for the maximum u_{rms} coincides with the position where the skewness is zero and the flatness has its minimum. This is also found in plane channel flow, as shown by Johansson & Alfredsson (1983), thereby stressing the close correspondence of the two types of flows in the near-wall region despite the large difference in Reynolds number between the flows.

A notable difference between simulation and experiment is found in the skewness factor $S(u)$ where the experimental data are consistently more negative than the DNS in the zone between the buffer region and the central plane. In the central plane $S(u)$ should be equal to zero due to the antisymmetry of the mean velocity profile and this is also observed in the experiment and the DNS. In the central plane of the channel the flatness factor $F(u)$ is almost 3 which is the value of a Gaussian distribution. The skewness and flatness factors of the remaining fluctuating

---

† Their data were recalculated using the friction velocity from the DNS giving $Re_\tau = 85.5$.

components determined from the simulation indicate that also these components are nearly Gaussian distributed in the centre of the channel.

No experimental data on the higher moments of the normal and spanwise components in plane Couette flow are found in the literature and also in plane Poiseuille flow similar data are scarce. Therefore, a comparison between our simulation and the DNS by Kim *et al.* (1987) at $Re_\tau = 180$ is of interest despite the difference by a factor of two in Reynolds number. There are notable differences between the two flows regarding $S(v)$ in the logarithmic region and $F(w)$ in the central plane. In Poiseuille flow, $S(v)$ has a local maximum in the logarithmic region. In plane Couette flow the flatness of w is close to 3 as shown in figure 6(*b*) whereas it is slightly above 3 in plane Poiseuille flow. The nearly Gaussian distribution found in the normal and spanwise velocity components in plane Couette flow is hence not found in plane Poiseuille flow. A source of discrepancy may be that the present numerical method tends to produce more Gaussian statistics than the more accurate spectral method applied by Kim *et al.*†

In figure 7 the constant total shear stress across the channel is separated into its turbulent and viscous contributions. Near the wall the turbulent shear stress increases proportionally to y^3 and has an almost constant level between $y = 50$ and the central plane, whereas the viscous shear stress decreases at the same rate. The product of the two terms is equal to the turbulence production which has its maximum where the curves intersect, i.e. at about $y = 10$. Figure 7 also shows that in the central plane both terms are finite and hence the turbulence production is finite throughout the whole flow field contrary to what is found in plane Poiseuille flow. In that flow the shear stress increases rapidly to a maximum near the wall and thereafter decreases almost linearly towards zero at the centre of the channel.

4.2. *Two-point correlations*

Two-point correlation coefficients were obtained from both experiments and DNS. The experiments consisted of LDV measurements at $Re = 1300$ with counter-moving walls and hot-film measurements at $Re = 1500$ with one moving and one stationary wall. Figure 8(*a,b*) shows correlation coefficients of the streamwise velocity component in the centreplane presented as a function of the streamwise and spanwise separation, respectively. In addition, hot-wire measurements by Robertson & Johnson (1970) at much higher Re (= 11 800) are included.

Figure 8(*a*) contains data from LDV and DNS. The data do not overlap but the main trend of the correlation is similar in both data sets. For the shortest separation distances the coefficient falls off rapidly and for the largest distances it levels out to an almost constant value which is above zero. A notable difference between the two sets of data is that in the experiments the correlation show considerably longer streamwise scales than in the DNS. The form of the correlation coefficients indicates a flow with a larger eddy size superposed on a spectrum of smaller eddy sizes as discussed by Townsend (1976). The data of Robertson & Johnson (1970) agree well with the data from the simulation for small separations where the high-*Re* data fall off as would be expected from a flow with a wide spectrum of eddy sizes. However the report does not contain any information about the hot-wire set-up. It is reasonable to believe that there is an influence on the downstream sensor by the upstream hot-wire probe.

---

† Higher-order moments such as skewness and flatness are significantly influenced by strong and intermittent turbulence events. These events have gradients at small length scales which second-order central differences tend to damp.
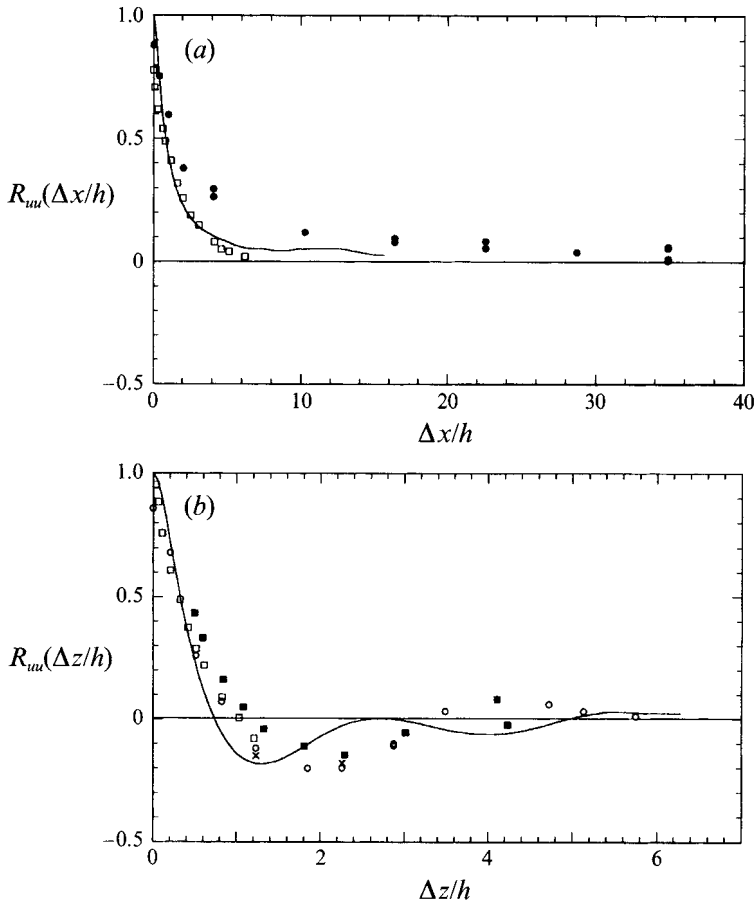
FIGURE 8. Correlation coefficient at the centreline. (a) Streamwise correlation: —, DNS; •, LDV. (b) Spanwise correlation: —, DNS; ○, LDV (unblocked channel); ×, LDV (blocked channel); ■, hot-film; □, Robertson & Johnson (1970), $Re = 11\,800$ (hot wire).

The spanwise correlation coefficient obtained from DNS, LDV and hot-film measurements are plotted in figure 8(b) (where the hot-film data were taken at $Re = 1500$). Both DNS and LDV data show a periodicity in the correlation but the former have a wavelength about 60% of that obtained from the latter. The zero crossing as well as the first minimum of the correlation coefficient from hot-film measurements are both slightly shifted towards a higher value in comparison to what is found from LDV. The wavelengths obtained from the hot-film and LDV seem to agree and the less emphasized extreme values in the hot-film data may be a consequence of having the probe axes in the spanwise direction. The measurements by Robertson & Johnson (1970) also contain spanwise correlation data which are plotted in the figure. Unfortunately their data are restricted to the spanwise separation $\Delta z/h < 1.25$. The few data points that are given fall close to the present experimental data and thus to some extent support the longer spanwise wavelength found in our experiments.

To ensure that the spanwise regularity in the correlation coefficient or its wavelength were not related to the channel entrance conditions the entrances were blocked and LDV measurements at three different positions were made. These data are plotted
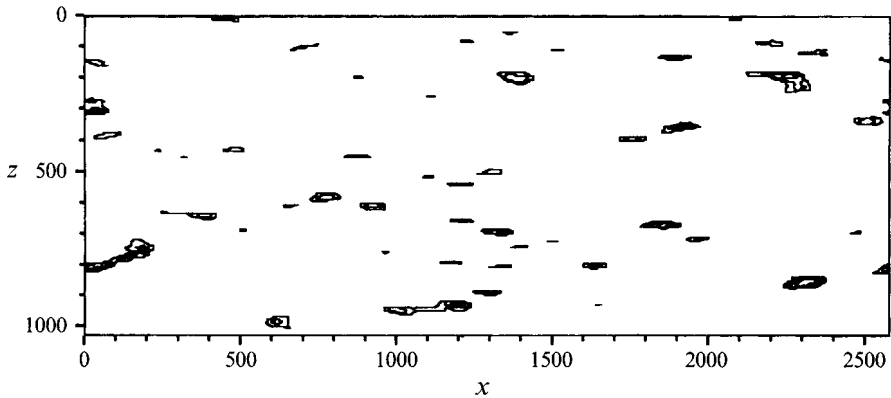
FIGURE 9. Contours of $var_u(x, z, t; L)$ at $y=13$. Contour increment is 0.5, lowest contour corresponds to unity variance.

in the figure and show that despite the drastic change of the entrance conditions no substantial effect on the correlation coefficient was found.

5. Coherent structures

5.1. *Structures detected by the VISA and VITA schemes*

In order to study flow structures in the near-wall region, the Variable Interval Space Averaging (VISA) and Variable Interval Time Averaging (VITA) techniques were employed on the numerical and experimental data bases, respectively. The VISA scheme detects an event when the local variance of u exceeds a specified threshold level. The local variance is defined as

$$var_u(x, z, t; L) = \frac{1}{\overline{u^2}} \left[\frac{1}{L} \int_{-L/2}^{L/2} u^2 \, dx - \left(\frac{1}{L} \int_{-L/2}^{L/2} u \, dx \right)^2 \right].$$

The overbar denotes averaging in the (x, z)-plane and over the available 12 flow fields in the data-base. The detection conditions applied were

$$var_u(x, z, t; L) \geqslant 1.0 \quad \text{and} \quad \frac{\partial u}{\partial x} < 0.0.$$

The latter criterion was applied where $var_u(x, z, t; L)$ had its maximum. The detection was carried out at $y = 13$ and L was chosen to give the maximum number of detections ($L = 170$).

In figure 9, $var_u(x, z, t; L)$ calculated from the DNS data-base is plotted for the first of the 12 flow fields in the data base. The areas inside the contours, hence the 'islands', were observed to move a distance comparable to their own length in the streamwise direction during a time interval of 12 t_*. During the motion, the topology of the islands changed little. The spanwise movement of the islands was marginal compared to the spanwise grid spacing Δz during 12 time units. Approximately 50–60 islands were detected at one instant in one (x, z)-plane.

In order to make comparisons between VITA and its spatial equivalent, the numerical spatial data must be represented as functions of time. (It is not feasible to record the velocity signal at a point in a DNS flow field because the time series must be very long and therefore extremely demanding concerning CPU time.) JAK calculated
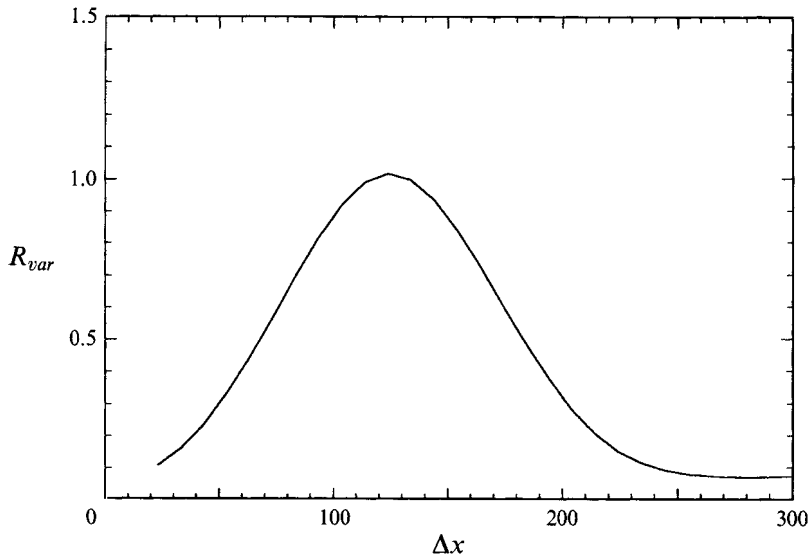
FIGURE 10. Space–time correlation ($\Delta T = 12$) of $var_u(x, z, t; L)$ from the DNS at $y = 13$. Integration length $L = 170$.

the mean propagation velocity c by tracking a number of individual VISA islands in time. The present approach was slightly different in that the space–time correlation

$$R_{var}(\Delta x; \Delta T, L) = \begin{cases} \overline{var_u(x, z, t; L) \times var_u(x + \Delta x, z, t + \Delta T; L)} / \overline{var_u(x, z, t; L)^2} \\ \text{(for } var_u(x, z, t; L) < 1.0, \; var_u(x, z, t; L) \text{ is set to 0)} \end{cases}$$

was calculated, see figure 10. Here ΔT equals the time interval between each of the fields in the data-base. The separation Δx_{max} corresponding to the maximum of R_{var} was utilized to calculate the propagation velocity $c = \Delta x_{max}/\Delta T = 10.4$. The mean velocity at $y = 13$ was 9.6; c was only weakly influenced by changing the integration length L. A 60% decrease in L caused the mean propagation velocity to change approximately 5%. The present approach is similar to that applied by Kim & Hussain (1993) for calculating propagation velocities of perturbations in turbulent Poiseuille flow. They concluded that the streamwise length scale of the perturbations had no significant influence on the propagation velocities. This is in agreement with the present results. The mean propagation velocity was calculated at $y = 3.8$ in order to investigate how c was influenced by the mean shear. At this position the propagation and mean velocities were 9.2 and 3.7, respectively. The present results support the view that the shear layers are structures with a well-defined propagation velocity which are only slightly deformed by the mean shear in the region $y < 20$.

Following the approach of Kim & Hussain (1993), the propagation velocity for pressure perturbations was calculated for the first 5 fields in the data-base. At $y = 13$, the propagation velocity was 12.6 which is in agreement with experimental findings (Schewe 1983). This implies that strong pressure perturbations are correlated with flow structures located further away from the wall than the ISL. From $y = 40$ and towards the centreplane, the pressure perturbations travelled with a velocity close to the mean.

A comparison between VITA and VISA results was obtained by plotting the number of events detected per unit time as a function of the integration time T, see figure 11. This quantity may be considered as an estimate of the 'bursting frequency'
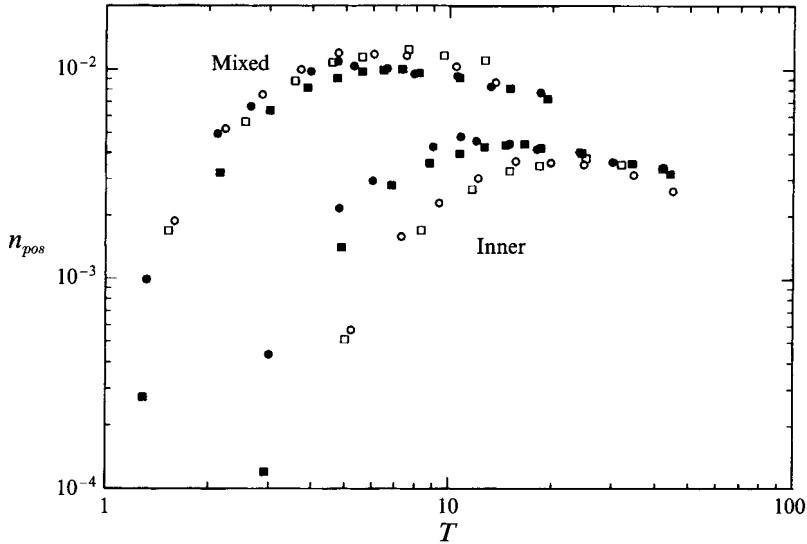
FIGURE 11. Frequency of occurrence of positive VISA and VITA events: ●, present experiment, $Re = 1260$; ■, present DNS, $Re = 1300$; ○, JAK, experiments; □, JAK, DNS.

(if the events detected by the VISA scheme are considered as identical to the 'bursts', see Robinson (1991) for a definition of 'burst'). The experimental Couette flow data were obtained with a single probe at $y = 13$. In order to compare experimental and numerical data, c was utilized to convert the spatial DNS data into temporal data in the same way as by JAK: the average number of detections per z-position was calculated from the DNS data-base as a function of L. The number of detections was then divided by L_x/c (L_x is the streamwise extent of the computational box). The comparison rests on at least two assumptions, namely that the shear-layer structures propagate with a velocity independent of integration time/length and that the effects of probe size/numerical resolution in the spanwise direction are negligible.

In addition to inner scaling, the mixed scaling suggested by Alfredsson & Johansson (1984) was applied. (Note that the axis labels in figure 11 do not correspond to a specific scaling.) The mixed time scale $t_m = (v/u_\tau^2)^{1/2}(h/U_w)^{1/2}$ seems to be the most appropriate choice since a better collapse between the Couette- and Poiseuille-flow results at different Re is achieved.

Figure 11 indicates that the agreement between experimental and numerical Couette flow data was good when T was larger than the value corresponding to the maximum number of detections in DNS ($T \approx 17$). The experiments indicated that the maximum number of detections occurred at $T = 11$. For very small T, resolution effects might have influenced both experiments and DNS data.

5.2. *Kinematics*

In order to study the structure of the shear layers, conditional averages were constructed by sampling DNS data centred around the peak of each island at $y = 13$. The ensemble consisted of data from all the 12 available flow fields. Because the time interval between the flow fields was shorter than the lifetime of the ISL, one event could be counted several times. By comparing averages of a reduced ensemble obtained at one instant with the total ensemble, no significant differences, except for a reduced smoothness, was found. The ensemble averages $\langle u \rangle$, $\langle v \rangle$, $-\langle uv - \overline{uv} \rangle$ and
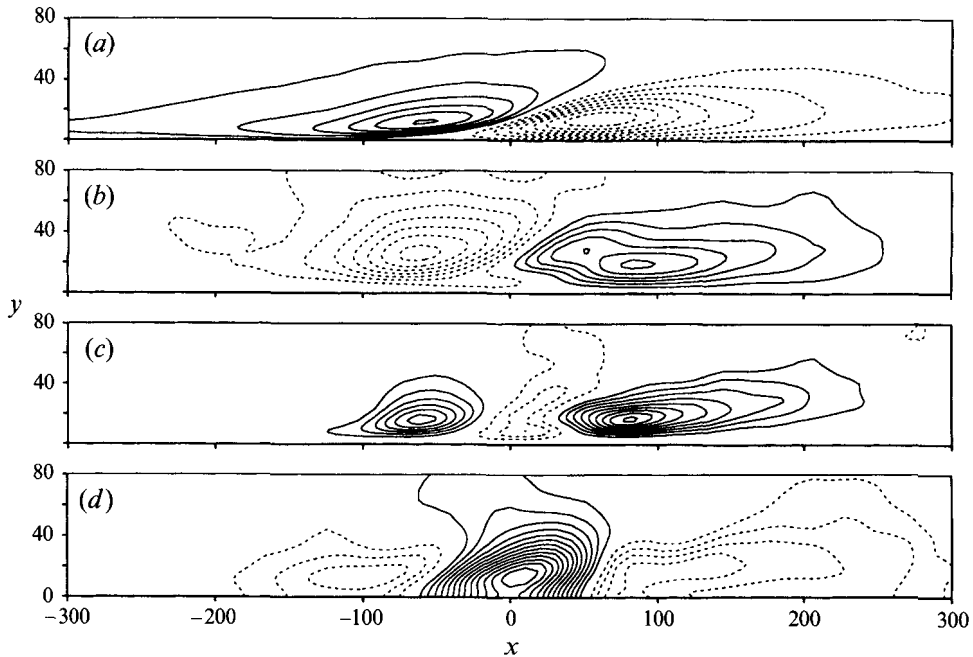
FIGURE 12. Ensemble averaged VISA events detected with $L=170$. Solid and broken lines denote positive and negative contours, respectively (zero contour not shown). (a) $\langle u \rangle$ (contour increment=0.5); (b) $\langle v \rangle$ (contour increment=0.1); (c) $-\langle uv - \overline{uv} \rangle$ (contour increment=0.2); (d) $\langle p - \overline{p} \rangle$ (contour increment=0.2).

$\langle p - \overline{p} \rangle$ in the (x,y)-plane are plotted in figure 12, the flow direction being from left to right. The slope of the ISL and the area of intense negative $\langle u \rangle$ connected with the outward motion in $\langle v \rangle$ are common features with the Poiseuille flow studied by JAK. The strong coupling of regions with simultaneously large values of $\langle u \rangle$ and $\langle v \rangle$ also gives as a result a high value of the conditionally averaged turbulent shear stress (c). Figure 12(d) also shows that the ISL is associated with a strong pressure pulse. According to Kim & Hussain (1993), the positive pressure peak is due to the 'slow pressure' while the areas of negative pressure surrounding it is associated with 'rapid pressure'. Here, rapid and slow refer to the terms in the Poisson equation for the pressure due to the mean field and the fluctuating velocities, respectively. Kim & Hussain pointed out that the fluctuating pressure is set up by the fluctuating velocity field in the whole channel. This gives pressure fluctuations a propagation velocity different from velocity and vorticity components.

Upstream of the centre of the ISL, the sweeping motion generates positive turbulent shear stress (quadrant 4 in the u,v-plane). Downstream of the ISL, the 'ejection' (quadrant 2 or Q2) is responsible for the main contribution to $-\langle uv - \overline{uv} \rangle$. The 'wall-ward interaction' (Q3) observed by JAK and located between the wall and $y = 15$, was also recognized in the present investigation as a small tongue of negative $\langle v \rangle$ extending into the domain of negative $\langle u \rangle$.

The low Reynolds number of the present DNS made the area of negative $\langle v \rangle$ in figure 12(b) extend from the channel centreplane to the wall. This was considered as a fundamental difference from the earlier Poiseuille flow study, in which the extent of the corresponding area in wall units was the same as in the present investigation, but the higher Reynolds number made the channel width more than twice as large. In the
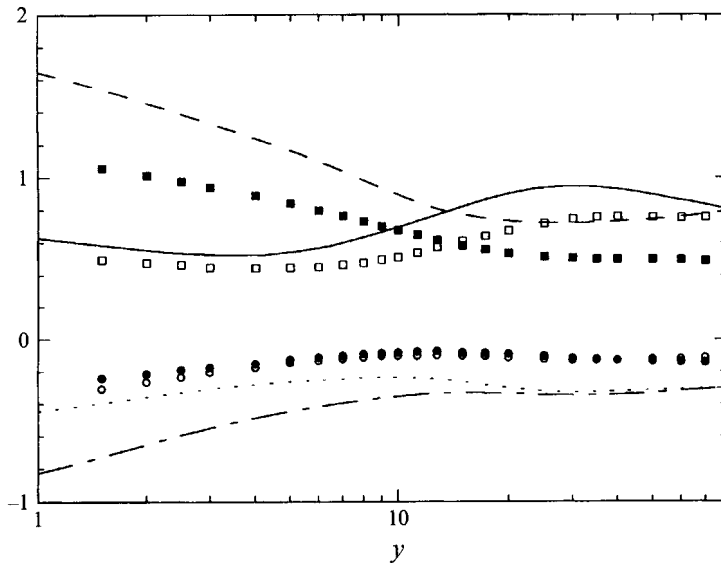
FIGURE 13. Fractional contributions to the turbulent shear stress. Present DNS of plane Couette flow compared with DNS of plane Poiseuille flow (Kim *et al.* 1987). Couette flow: present DNS; — - , Q1; — , Q2; · · ·, Q3; - - - , Q4. Poiseuille flow, KMM: ○, Q1; □, Q2; ●, Q3; ■ , Q4.

study by JAK the sweeping motion was confined to the viscous sub-layer and buffer zone. The present results show that the 'sweep' extends from the viscous sub-layer to the central region. As a consequence of this, the fluctuations in both u and v are stronger on the upstream side of the ISL compared to those of the Poiseuille flow. The peak-to-peak value in figure 12(a) was, however, practically equal to the corresponding value in JAK. This is not surprising since the same detection criterion and threshold were applied in the two studies.

Although the velocity components displayed a behaviour similar to the corresponding quantities in the Poiseuille flow study, the conditionally averaged turbulent shear stress in figure 12(c) revealed a significant discrepancy due to the stronger emphasis on the sweep: $-\langle uv - \overline{uv} \rangle$ was more symmetrically distributed with respect to the centre of the ISL structure in the present investigation. The peak value of the shear stress on the upstream side of the centre of the ISL was found to be 2/3 of the peak on the downstream side.

A comparison between the fractional contributions to the turbulent shear stress (in the long-time averaged sense) from the different quadrants in Couette and Poiseuille flow (Kim *et al.* 1987, $Re_\tau = 180$) is displayed in figure 13. Considering Q2 and Q4 events, the qualitative behaviour was similar between the two flows for $y < 30$. In Couette flow, however, the Q4 contribution was relatively more important close to the wall. At the centreline, Q2 and Q4 change their roles (as do Q1 and Q3) in Couette flow due to the antisymmetry of the mean velocity profile. The point where the Q2 and the Q4 curves intersect was at nearly the same location in the two different flows. A general feature seemed to be that both the positive and negative contributions were relatively more influential in the shear-driven Couette flow than in the pressure-driven Poiseuille flow.

In figure 14, $\langle u \rangle$, $\langle v \rangle$, $-\langle uv - \overline{uv} \rangle$ are visualized in 3 different (x, z)-planes. The increment between the contour levels had to be decreased to half of that in figure 12 in order to visualize the structures in the viscous sub-layer. The detection was carried
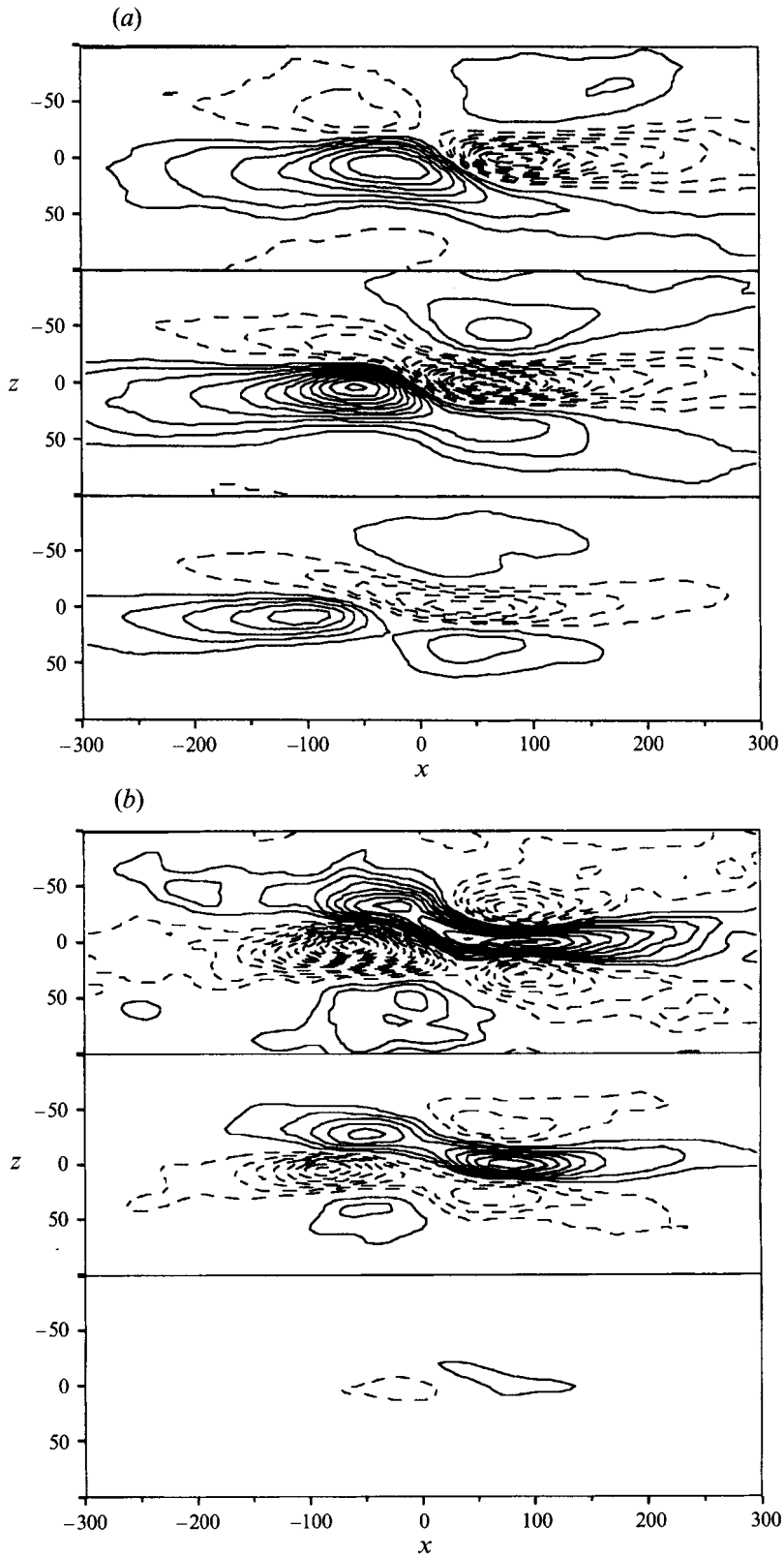
(a)

(b)

FIGURE 14 (a,b). For caption see facing page.
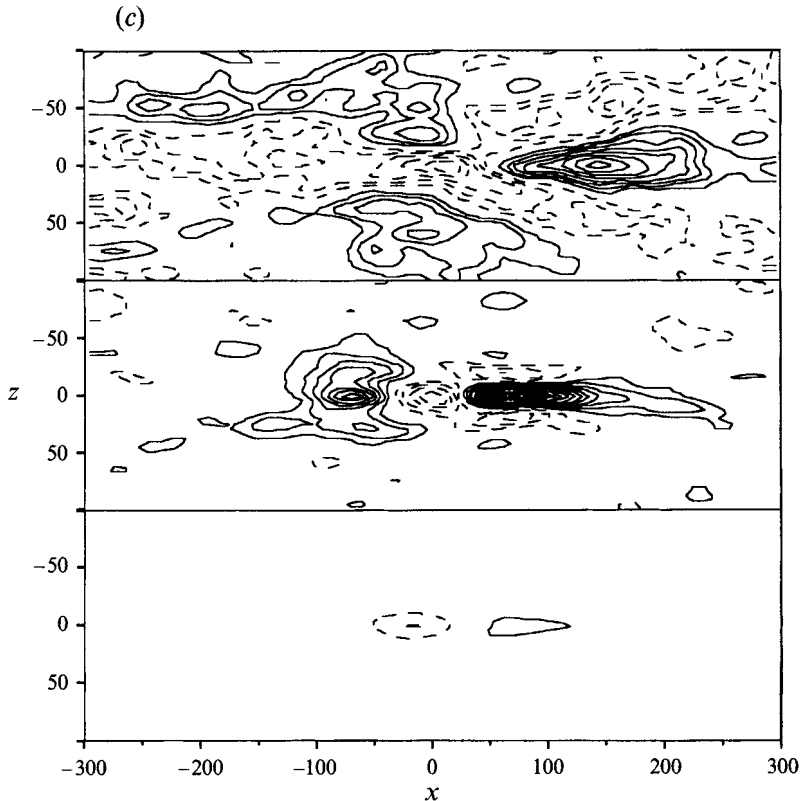
(*c*)

FIGURE 14. Ensemble-averaged events in the (x, z)-plane, at $y = 4$ (lower), 13 (middle), 25 (upper). $L = 170$. (*a*) $\langle u \rangle$ (contour increment=0.25); (*b*) $\langle v \rangle$ (contour increment=0.05); (*c*) $-\langle uv - \overline{uv} \rangle$ (contour increment=0.1).

out at $y = 13$ as in the preceding visualizations. The sloping nature of the ISL can be seen in figure 14(*a*) where the centre of the structure shows that it is inclined in the downstream direction. In order to preserve the skewed instantaneous structure of u and v, these velocity components were ensemble averaged so that the spanwise asymmetry of each sample was preserved, i.e. the sample was mirrored in the (x, y)-plane if the spanwise derivative of u at the detection point was negative. Figure 14(*b*) reveals that the ejection and the sweep are more elongated in the flow direction than can be inferred from figure 12 due to the angle between the ISL and the mean flow. The skewed nature of the structures contradicts the simple picture (e.g. Kim *et al.* 1971) of a sweep following an ejection.

The contribution to the conditionally averaged turbulent shear stress in figure 14(*c*) from the upstream part of the ISL appears smeared out compared to the localized peak on the downstream side. At $y = 24.5$, the contributions to $-\langle uv - \overline{uv} \rangle$ in the regions associated with positive $\langle v \rangle$ upstream of the centre of the ISL are significant, showing how the structure of the shear layer changes and becomes more complex as the observer moves from the wall towards the channel centre. This increasing emphasis on Q2-events is clearly seen in figure 13, and is a common feature with the Poiseuille flow. However, as the channel centre is approached and the long-time-averaged turbulent shear stress approach a high, almost uniform level, the VISA-detected events will become relatively less important contributors to the shear stress.

Nishino & Kasagi (1991) found from particle tracking velocimetry that two pairs of counter-rotating vortices generate the ISL. The streamwise extent of the vortices was approximately 300. The first pair is associated with the sweeping motion and the second, downstream pair with the ejection. However, it is an inherent feature of one-point detection schemes that the structures will be symmetric in the spanwise direction, i.e. pairs of counter-rotating vortices will always be detected. Guezennec, Piomelli & Kim (1989) applied quadrant detection to DNS data for Poiseuille flow and found that when the spanwise asymmetry of the single events were taken into account in the conditional averaging, one rather than two vortical structures was observed. In order to investigate whether the present VISA-detected structures were associated with streamwise vortices, conditional averages of the spanwise and wall-normal velocities were constructed in three different (y, z)-planes in figure 15. The asymmetry of the individual events were taken care of using the same procedure as in figure 14. At $x = -100$, weak vortical structures associated with the sweep are seen. The vortical structures were inclined in the same way as the ISL in figure 12(a) and can be recognized further away from the wall at $x = 0$. On the downstream side of the ISL in figure 15(c), weak, asymmetric vortical structures are observed rotating in the opposite direction. The dominating features in figure 15(a,b) are, however, the sweep (a) and the spanwise outrush (b) between the vortical structures and the wall.

5.3. *Dynamics*

The importance of the VISA-detected events for the dynamics of wall turbulence was investigated by considering the production $\mathscr{P}$ of turbulent kinetic energy. The pressure–strain correlation occurring in the transport equations for the Reynolds stresses was studied to give further information on physical mechanisms acting in the ISL.

The conditionally averaged production is expressed as

$$\langle \mathscr{P} \rangle = -\langle uv \rangle \frac{\mathrm{d}U}{\mathrm{d}y} - \overline{u^2} \left\langle \frac{\partial u}{\partial x} \right\rangle - \overline{uv} \left\langle \frac{\partial u}{\partial y} + \frac{\partial v}{\partial x} \right\rangle - \overline{v^2} \left\langle \frac{\partial v}{\partial y} \right\rangle - \overline{w^2} \left\langle \frac{\partial w}{\partial z} \right\rangle. \quad (5.1)$$

The term on the left-hand side and the first two terms on the right-hand side of (5.1) are displayed in figure 16. The main contributions to $\langle \mathscr{P} \rangle$ come from these two terms. The first term is similar to the conventional time-averaged production term and the second term is dependent on the non-zero streamwise velocity gradient associated with the ISL. The positive production can be identified in three regions associated with the sweep, the shear-layer interface and the ejection, respectively. The production taking place on the upstream side of the ISL due to $-\langle uv \rangle$ is relatively large in Couette flow compared to what was found by JAK. In Couette flow, the sum of the terms, $\langle \mathscr{P} \rangle$ in figure 16(a), is very similar to that found in Poiseuille flow. The integration length applied in the present investigation is approximately 20% shorter than that applied by JAK, resulting in a slightly stronger production associated with $\langle \partial u/\partial x \rangle$ in the present investigation. A region with negative production associated with negative turbulent shear stress is observed close to the wall in the region occupied by the wall-ward interaction (see figure 12b).

Following JAK, the production terms were integrated over (x, z)-planes extending 293 and 44 wall units in the streamwise and spanwise directions, respectively. These planes were centred around the peak of each island. This procedure was carried out at different y-values from one wall ($y = 0$) to the other ($y = 164$) while the detection was carried out at $y = 13$. The latter stage was different from the method applied by JAK, but was thought to give more information on how the conditionally averaged
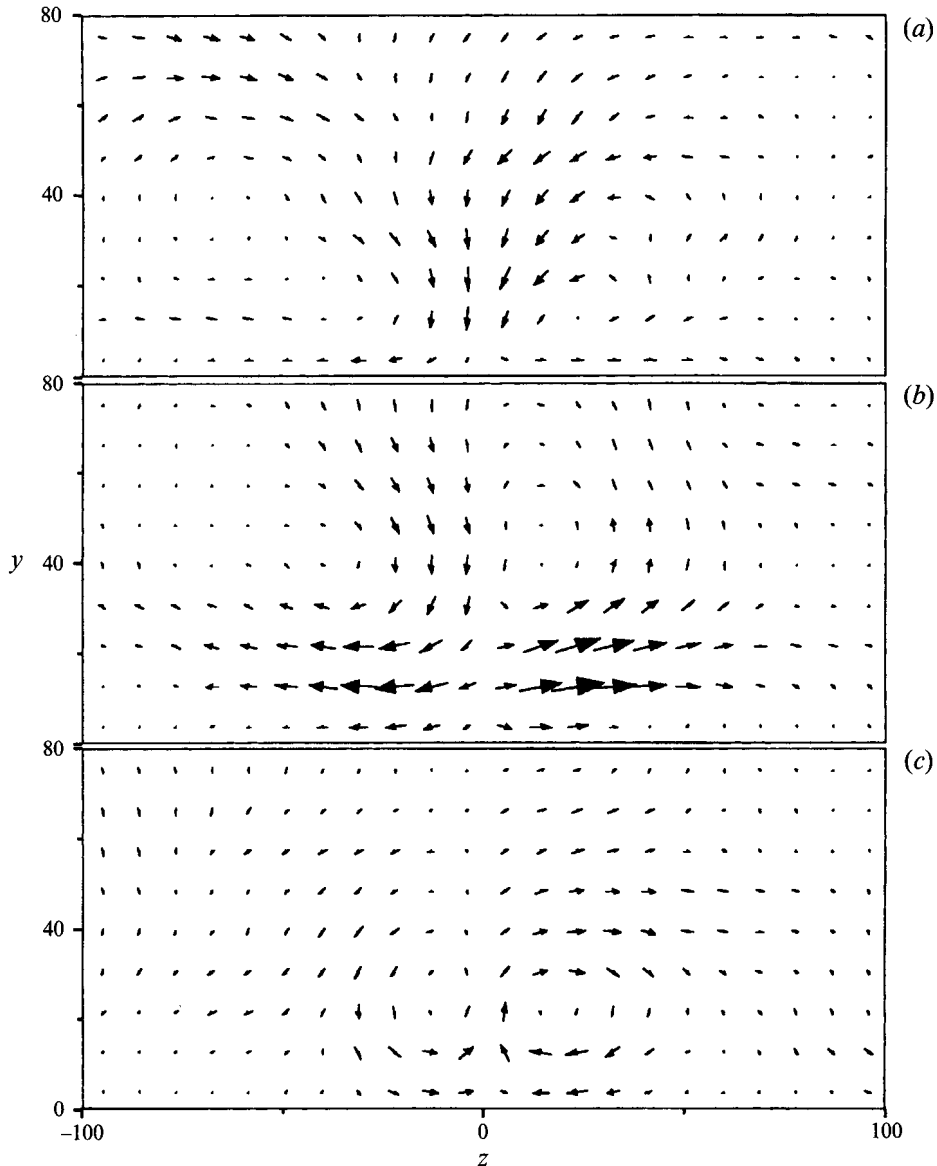
FIGURE 15. Cross-flow velocity vectors of ensemble-averaged events. (*a*) $x = -100$, (*b*) $x = 0$, (*c*) $x = +100$. The vectors do not represent the actual numerical resolution.

terms are connected to the conventionally averaged terms. Because the magnitude of $\langle \mathscr{P} \rangle_{xz}$† will depend on the area of the averaging plane (here 293 by 44), some care must be taken when interpreting the results displayed in figure 17.

The detection was carried out at $y = 13$ and the conditionally averaged production exceeded the long-time-averaged production at this side of the channel ($y < 82$). In the other half of the channel, however, the turbulence was not significantly affected by the specific structures near the opposite wall and only the first term on the right-hand side of (5.1) was significant, approaching the long-time-averaged value.

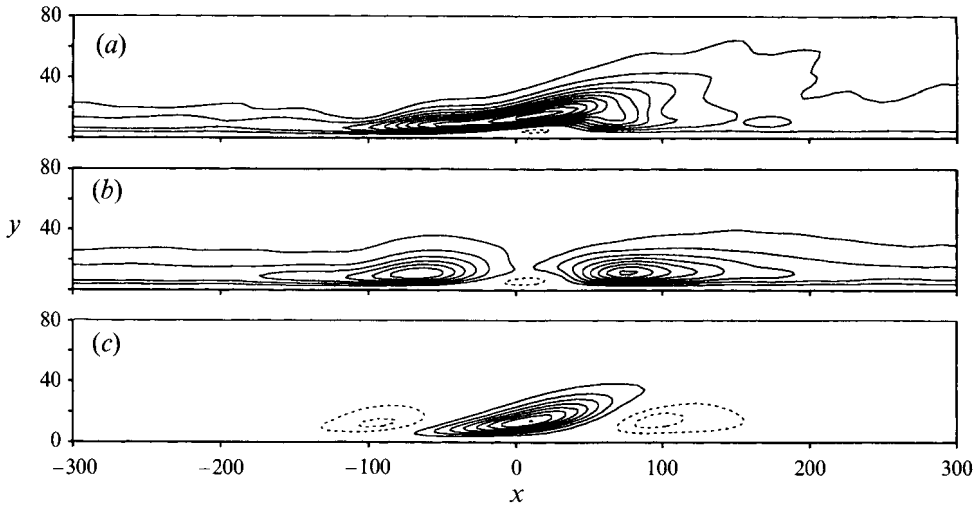† The subscript denotes averaging in (x, z)-planes of the specified size.

FIGURE 16.   Energy production in the shear layer (contour increment = 0.1): (a) total conditional averaged production $\langle \mathscr{P} \rangle$, (b) Reynolds-stress-associated production $-\langle uv \rangle dU/dy$, (c) $-\overline{u^2}\langle \partial u/\partial x \rangle$.
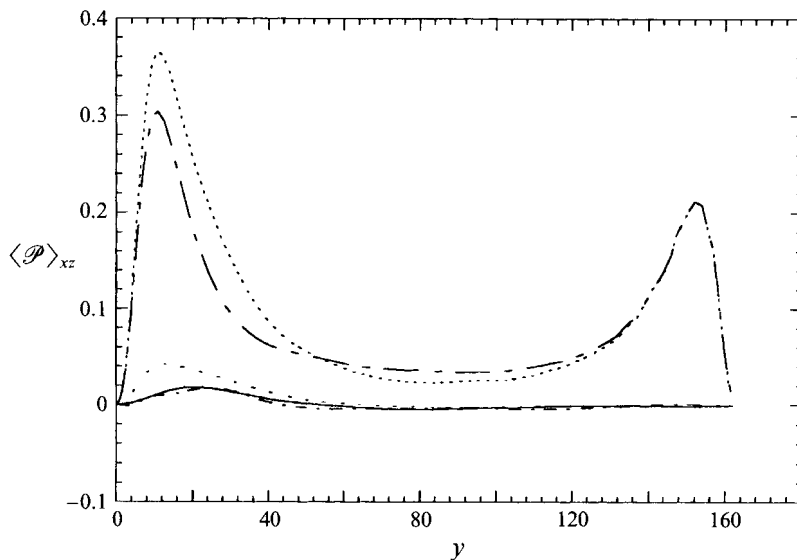

FIGURE 17. Conditional-averaged energy production terms. Integration area in the (x,z)-plane is 293×44, detection at $y = 13$ (walls are at $y = 0$ and $y = 164$). $\cdots$, $\langle \mathscr{P} \rangle_{xz}$; — —, $-\langle uv \rangle_{xz} dU/dy$; - - -, $-\overline{u^2}\langle \partial u/\partial x \rangle_{xz}$; — - - — -, $-\overline{uv}\langle \partial u/\partial y \rangle_{xz}$; — , $\overline{w^2}\langle \partial w/\partial z \rangle_{xz}$.

The second term in (5.1) depends on the ensemble-averaged velocity gradient which is approximately proportional to the integration length L. However, because the number of events detected will decrease if L is changed, the present qualitative behaviour will be retained. Following JAK, $\langle \mathscr{P} \rangle_{xz}$ was integrated from $y = 0$ to $y \approx 30$ and it was found that the production per unit volume in the regions occupied by the ISL was approximately 3 times as large as the production in the rest of the volume.

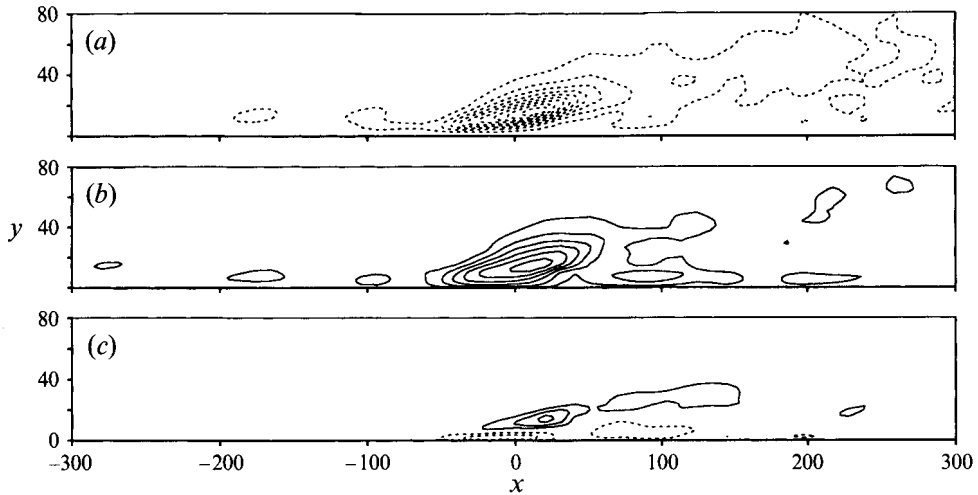The VISA-detection scheme triggers in areas with large streamwise gradients of u,

FIGURE 18. Diagonal components of the conditionally averaged redistribution tensor (contour increment $= 0.1$). (a) $\langle\phi_{11}\rangle$; (b) $\langle\phi_{33}\rangle$; (c) $\langle\phi_{22}\rangle$.

but in addition, the turbulent shear stress and the pressure display significant localized peaks. While the shear stress contributes to the production of k, the pressure–strain correlation is responsible for the redistribution of k between the turbulent normal stresses. The physical mechanisms underlying the redistribution and its connection with the production may, however, be understood by studying the dynamics of coherent structures. Considering here only the diagonal components, it was found that the ISL were significant contributors to the conditionally averaged redistribution terms

$$\langle\phi_{ij}\rangle = \left\langle \frac{p}{\rho} \left(\frac{\partial u_i}{\partial x_j} + \frac{\partial u_j}{\partial x_i} \right) \right\rangle. \tag{5.2}$$

The terms† are visualized in the (x, y)-plane in figure 18. The loss of kinetic energy from the mean flow results in a gain in $\langle u^2\rangle$, implying that $\langle\phi_{11}\rangle$ is negative in order to redistribute energy to $\langle v^2\rangle$ and $\langle w^2\rangle$. The strong influence of the specific structures (as detected by the VISA-scheme) was obvious since the redistribution was significant only in the same region as the production due to $-\overline{u^2}\langle\partial u/\partial x\rangle$, see figure 16(c). The redistribution seems to be associated with strongly localized production occurring in connection with ISL/pressure pulses rather than production associated with turbulent shear stress.

The energy was mainly redistributed from $\langle u^2\rangle$ into $\langle w^2\rangle$ as can be inferred from $\langle\phi_{33}\rangle$. Figure 15(b) shows that $\langle\partial w/\partial z\rangle$ was large compared to $\langle\partial v/\partial y\rangle$ at the centre of the ISL. This observation justifies that $\langle\phi_{33}\rangle$ was larger than $\langle\phi_{22}\rangle$ and that the maximum redistribution occurred around the plane displayed in figure 18 ($z = 0$). $\langle v^2\rangle$ was reinforced in the outer part of the ISL but was strongly damped close to the wall where energy was fed into $\langle w^2\rangle$. The magnitude of $\langle v^2\rangle$ was very small in the immediate vicinity of the wall while $\langle\phi_{22}\rangle$ was significant and negative. This negative

† A central-difference approximation of the analytically obtained terms in (5.1) and (5.2) does not correspond exactly to the production and redistribution terms obtained from the discretized momentum equations as they appear in DNS codes. The time-averaged proper calculated production was approximately 10% higher than indicated by figure 17, while the proper time-averaged redistribution terms show good agreement with figure 19.
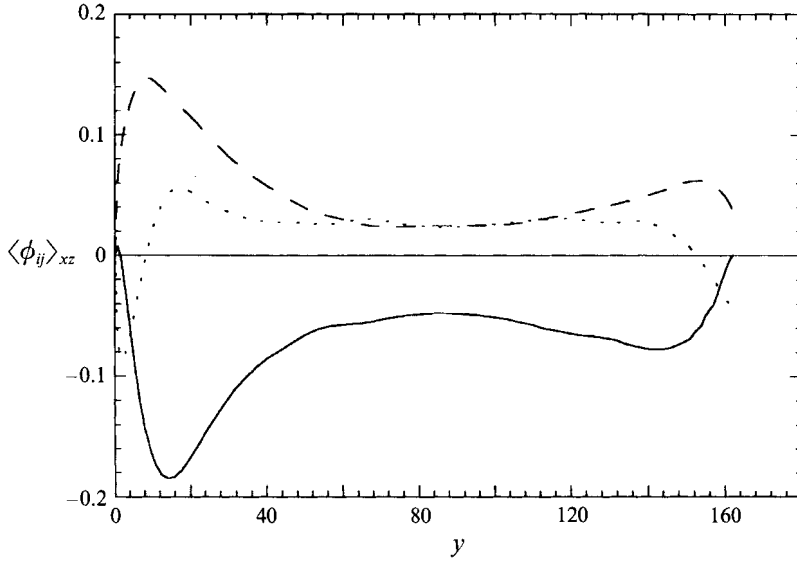
FIGURE 19. Conditional-averaged redistribution terms. ——, $\langle \phi_{11} \rangle_{xz}$; $\cdots$, $\langle \phi_{22} \rangle_{xz}$; - - -, $\langle \phi_{33} \rangle_{xz}$.

redistribution was a result of the high wall pressure and the wall-ward interaction (figure 12*b,d*).

The significance of $\langle \phi_{ij} \rangle_{xz}$ can be estimated from figure 19, where the same plane-averaging procedure as applied to $\langle \mathscr{P} \rangle_{xz}$ is utilized. From a qualitative viewpoint the behaviour of the conditionally averaged redistribution was similar to that of the long-time-averaged redistribution. $\langle \phi_{ij} \rangle_{xz}$ had a higher magnitude than the long-time average in the region where the ISL were detected, indicating that the ISL are important in this physical process. Approximately 25% of the production of $\langle u^2 \rangle$ is redistributed to $\langle v^2 \rangle$ and $\langle w^2 \rangle$.

6. Discussion and conclusions

6.1. *The time-averaged turbulence field*

A few numerical and experimental investigations have previously been reported on turbulent plane Couette flow. However, long-time statistics of the flow field have not been reported in detail and until the present study no information on the near-wall coherent structures has been available.

The numerical simulation by Lee & Kim (1991) suggests that there are problems associated with numerical simulations of plane Couette flow, which are of a more severe nature than in plane Poiseuille flow. The simulations reported by Bech & Andersson (1994) suggested that at least two realizations of the flow field are possible, the results depending on the size of the computational box and the ratio L_x/L_z and also on the duration of the simulations. In the following, the two realizations will be referred to as the 'periodic state' (which is similar to the flow state obtained by Lee & Kim) and the 'disordered state' (similar to the present DNS) referring to the appearance of the large-scale field.

Until the present DNS data became available, the experimental results were compared with numerical data from a preceding simulation with a coarser grid in the spanwise direction and a differently sized computational box. The computational box

was 1.6 times larger in the streamwise direction and half as wide in the spanwise direction compared to the present simulation. The simulation was run for a time of 330 t_* and strong large-scale eddies corresponding to the periodic state were observed. The scales of these eddies were more similar to the experimentally observed quantities than those inferred from the comparison between the two-point correlations in §4.2. However, the periodic state was observed to be associated with a continuous forcing of the eddies, resulting in a higher level of the turbulent kinetic energy. The near-wall streak spacing was significantly increased by the influence of the large-scale eddies.

The discrepancies between the experimentally and numerically obtained two-point correlations of u were associated with the size of the large scales. The extremely large eddies observed in Couette flow made numerical simulations difficult. The present experiments gave a similar spanwise wavelength for the central streaks to that found by Lee & Kim (1991). The extremely large streamwise scales present in the experiments using two moving walls may be due to the zero mean flow, i.e. the structures are not convected out of the channel. This may also be the explanation for the fact that the experimentally obtained mean shear exhibited a lower value in the central region compared to the numerical data. This would give a lower turbulence production rate ($\mathscr{P}$) which is consistent with the lower level of u_{rms} in the experiment as compared to the simulation in the central region.

In a large-eddy simulation using the same computational box as the present DNS, but with a coarser grid, a change from the periodic to the disordered state was observed with a time scale of the order 800 t_*. A possible explanation of this observation is that the numerical solution of the flow problem is extremely sensitive to disturbances and that the periodic state was a result of the disturbances associated with the initial flow field. Then, after the simulation had been run for a relatively long time, the turbulence entered the disordered state. Following this argument, it may be assumed that an experimental realization of the Couette flow, which will include some kind of inlet disturbance, will tend to the periodic state but without suffering from the continuous forcing and other shortcomings observed in numerical simulations.

Couette flow has different symmetry properties as compared to Poiseuille flow. This gives rise for instance, to the skewness of u being zero at the centreline. The Reynolds shear stress has a maximum at the centreline and is not zero as in Poiseuille flow and the turbulence production is finite over the full width of the channel. This also gives rise to a much higher turbulence intensity in the central part of the channel and for instance v_{rms} is twice as high in the present computation at the centreline compared to that obtained by Kim *et al.* (1987). Therefore it is hard to draw any firm conclusions from a comparison of the present data in the outer flow region with that of other wall-bounded flows. However, the agreement in the near-wall region between the present experimental and numerical data was excellent concerning the mean velocity and the second- and higher-order moments of u. Also comparisons with other wall-bounded flows showed that in the long-time-averaged sense these types of flows are very similar.

The present numerical data for the skewness factors of u and v in the region $y > 40$ suggested that this (approximately logarithmic) region is less dominated by ejections than is the case in Poiseuille flow. This tendency was also observed in the quadrant splitting of the turbulent shear stress. In Couette flow Q2 and Q4 events change roles at the centreline due to the constant mean shear. In Poiseuille flow, the Q2 (ejection) contribution is the most significant in the logarithmic region.

The stronger influence of the outer region (and the opposite half-channel) in Couette flow compared to Poiseuille flow may contribute to explain the differences in

$-\langle uv - \overline{uv} \rangle$. This difference was mainly associated with a stronger sweeping motion in Couette flow, resulting in a more symmetrical distribution of $-\langle uv - \overline{uv} \rangle$ with respect to the centre of the ISL. The low Re of the present flow made the outer region become more dominant than in the Poiseuille flow with Re more than twice as high.

The difficulties in representing the large-scale eddies of Couette flow numerically were not solved in the present DNS. However, the simulation was considered to be consistent with respect to the periodic boundary conditions because the two-point correlations were close to zero at separations corresponding to half the box size. The good agreement in the near-wall region with both experiments and other wall-bounded flows suggests that an investigation of near-wall structures using the numerical and experimental data is worthwhile.

6.2. Near-wall structures

The ISL which were the focus of our study of near-wall structures were found to have a propagation velocity ($c = 10.4$) which was close to that of Poiseuille flow (JAK). The method used here was somewhat different from the one used by JAK but was computationally more direct. The present values of c are 2–3% lower than the propagation velocity of u-perturbations found by Kim & Hussain (1993) from long-time correlation data. Their investigation showed that the propagation velocities collapsed with the mean velocity when $y > 20$, whereas the perturbations are wave-like in the vicinity of the wall. Guezennec *et al.* (1989) calculated the propagation velocity for quadrant-splitting detected events. The sweeps (Q4 events) were found to travel faster than the ejections (Q2), the propagation velocities being 10.3 and 9.3, respectively. The good agreement between the propagation velocities of VISA events, Q4 events and perturbations suggests that the coherent structures considered in the different studies are closely linked to each other. The somewhat higher propagation velocity of pressure perturbations (here 12.6) was also detected by Kim & Hussain.

The VITA and VISA techniques displayed a reasonable agreement in the number of events detected. By applying mixed scaling, the present data collapsed quite well with the results of JAK at a higher Reynolds number, especially for short integration times. For long integration times, several structures will pass while the time window is open, and the results become ambiguous. Because of the different nature of the two flows, the agreement was considered to be good and it seems plausible to expect that the Reynolds number dependence is removed from the data by applying the mixed scaling. Shah & Antonia (1989) did experiments in Poiseuille flow at Reynolds numbers ranging from 3300 to 33 000 and found that mixed scaling was the most appropriate at higher Reynolds numbers. At lower Reynolds numbers they found that inner scaling gave a better collapse of data. The discrepancy between their findings and the present results may be due to the different flow cases and the different Re considered.

The structure of the ISL detected was found to resemble the corresponding results given by JAK. The structures were longer in the study by JAK. This discrepancy may be a Reynolds number effect, but also a result of the shorter L applied in the present investigation. The more symmetric distribution of the turbulent shear stress has already been discussed in connection with more general features of the Couette flow. The peak value of the shear stress on the upstream side of the centre of the ISL was found to be 2/3 of the peak at the downstream side, whereas the corresponding ratio in JAK was 1/6. In addition, the peak-value of $-\langle uv - \overline{uv} \rangle$ was 25% lower than in the Poiseuille flow study. Even though the long-time-averaged turbulent shear

stress does not exhibit a maximum near the wall (as in Poiseuille flow), $-\langle uv - \overline{uv} \rangle$ does.

In the immediate vicinity of the wall in Couette flow, Q1 is seen to give a strong negative contribution as compared to Q3, in contrast to what is observed in Poiseuille flow. Q1 is associated with outward motion of low-speed fluid. It is plausible to assume that this is the result of a reflection from the wall of an inward motion of low-speed fluid (note that for a moving wall 'high' and 'low' change meaning as compared to a non-moving wall). If a relatively strong sweep and a resulting strong reflection are postulated, then these phenomena will contribute to the explanation of the discrepancy in $-\langle uv - \overline{uv} \rangle$ between the present study and JAK because the sweep adds to the conditionally averaged turbulent stress in the upstream part of the ISL whereas the reflection reduces it in the downstream region. The idea of a relatively strong reflection is supported by the fact that the pressure pulse in figure 12(*d*) is 40% stronger in the present study compared to the results by JAK.

Visualizations of the present numerical data indicate that possible streamwise vortices associated with the ISL are not distinct like the structures detected by Nishino & Kasagi (1991) and it is not clear whether the vortical structures occur as single structures or in pairs. However, the vortical structures seem to meander in the spanwise direction and the sign of the streamwise vorticity changes in the centre of the ISL.

The present results do partly agree with the findings of Brooke & Hanratty (1993) obtained using instantaneous visualizations of a Poiseuille flow DNS. Brooke & Hanratty observed that a near-wall vortex was 'born' downstream relative to the position where a stress-producing eddy lifts away from the wall. This lifting was found to be associated with 'large spanwise flow at the wall' and a pressure pulse. The spanwise motion then triggers the birth of a near-wall vortex with vorticity of the opposite sign. This regeneration process suggested by Brooke & Hanratty seems to be compatible with the present results. It should, however, be stated that conditionally averaged quantities do not necessarily correspond to instantaneous flow structures. The spanwise extent of the vortical structures (and the ISL) in the present investigation compare reasonably well with the results of Guezennec *et al.* (1989), Brooke & Hanratty and Nishino & Kasagi (1991).

Hamilton, Kim & Waleffe (1993) examined the regeneration of turbulence in a minimal-box DNS of Couette flow. They observed that *x*-independent streaks become skewed and break up as a part of the regeneration cycle. The 'wavy' unstable streak in their investigation resembles the ISL.

The production of turbulent kinetic energy associated with the ISL was significant. Sweep, ejection and shear-layer interface all contributed to the conditionally averaged production. The present results were similar to those of JAK and the importance of the ISL in the overall production was found to be approximately equal in the two investigations. However, the sweep was responsible for a relatively large contribution to the production in the present investigation.

The ensemble-averaged flow variables offered a spatial description of the redistribution process. The redistribution of turbulent kinetic energy between the normal Reynolds stresses was found to take place mainly along the shear-layer interface. In this region, the production is due to terms that average to zero in the long-time sense.

REFERENCES

ALFREDSSON, P. H. & JOHANSSON, A. V. 1984 Time scales in turbulent channel flow. *Phys. Fluids* **27**, 1974.

ANDERSSON, H. I. & KRISTOFFERSEN, R. 1992 Statistics of numerically generated turbulence. *Acta Appl. Math.* **26**, 293.

AYDIN, E. M. & LEUTHEUSSER, H. J. 1979 Novel experimental facility for the study of plane Couette flow. *Rev. Sci. Instrum.* **50** (11), 1362.

AYDIN, E. M. & LEUTHEUSSER, H. J. 1987 Experimental investigation of turbulent plane-Couette flow. *ASME Forum on Turbulent Flows*, FED vol. 51, p. 51.

AYDIN, E. M. & LEUTHEUSSER, H. J. 1991 Plane-Couette flow between smooth and rough walls. *Exps Fluids* **11**, 302.

BECH, K. H. & ANDERSSON, H. I. 1994 Very-large-scale structures in DNS. In *Direct and Large-Eddy Simulation I.* (ed. P. R. Voke, L. Kleiser & J.-P. Chollet), p. 13. Kluwer.

BLACKWELDER, R. F. & KAPLAN, R. E. 1976 On the wall structure of the turbulent boundary layer. *J. Fluid Mech.* **76**, 89.

BROOKE, J. W. & HANRATTY, T. J. 1993 Origin of turbulence-producing eddies in a channel flow. *Phys. Fluids* A **5**, 1011.

CLEVER, R. M. & BUSSE, F. H. 1992 Three-dimensional convection in a horizontal fluid layer subjected to a constant shear. *J. Fluid Mech.* **234**, 511.

EL TELBANY, M. M. M. & REYNOLDS, A. J. 1982 The structure of turbulent plane Couette flow. *Trans. ASME* I: *J. Fluids Engng* **104**, 367.

GAVRILAKIS, S. 1992 Numerical simulation of low-Reynolds number turbulent flow through a straight square duct. *J. Fluid Mech.* **244**, 101.

GAVRILAKIS, S., TSAI, H. M., VOKE, P. R. & LESLIE, D. C. 1986 Large-eddy simulation of low Reynolds number channel flow by spectral and finite difference methods. *Not. Numer. Fluid Mech.* **15**, 105.

GUEZENNEC, Y. G., PIOMELLI, U. & KIM, J. 1989 On the shape and dynamics of wall structures in turbulent channel flow. *Phys. Fluids* A **1**, 764.

HAMILTON, J. M., KIM, J. & WALEFFE, F. 1993 Regeneration of near-wall turbulence structures. *9th Symposium on Turbulent Shear Flows, Kyoto*, paper 11-5.

JOHANSSON, A. V. & ALFREDSSON, P. H. 1982 On the structure of turbulent channel flow. *J. Fluid Mech.* **122**, 295.

JOHANSSON, A. V. & ALFREDSSON, P. H. 1983 Effects of spatial resolution on measurements of wall-bounded turbulent shear flows. *J. Fluid Mech.* **137**, 409.

JOHANSSON, A. V., ALFREDSSON, P. H. & KIM, J. 1991 Evolution and dynamics of shear-layer structures in near-wall turbulence. *J. Fluid Mech.* **224**, 579 (referred to herein as JAK).

KIM, H. T., KLINE, S. J. & REYNOLDS, W. C. 1971 The production of turbulence near a smooth wall in a turbulent boundary layer. *J. Fluid Mech.* **50**, 133.

KIM, J. & HUSSAIN, F. 1993 Propagation velocity of perturbations in turbulent channel flow. *Phys. Fluids* A **5**, 695.

KIM, J., MOIN, P. & MOSER, R. 1987 Turbulence statistics in fully developed channel flow at low Reynolds number. *J. Fluid Mech.* **177**, 133.

KLINE, S. J., REYNOLDS, W. C., SCHRAUB, F. A. & RUNSTADLER, P. W. 1967 The structure of turbulent boundary layers. *J. Fluid Mech.* **30**, 741.

KRISTOFFERSEN, R. & ANDERSSON, H. I. 1993 Direct numerical simulations of low Reynolds number turbulent flow in a rotating channel. *J. Fluid Mech.* **256**, 163.

KRISTOFFERSEN, R., BECH, K. H. & ANDERSSON, H. I. 1993 Numerical study of turbulent plane Couette flow at low Reynolds number. *Appl. Sci. Res.* **51**, 337.

LEE, M. J. & KIM, J. 1991 The structure of turbulence in a simulated plane Couette flow. *8th Symposium on Turbulent Shear Flows, Munich*, paper 5-3.

MIYAKE, Y., KAJISHIMA, T. & OBANA, S. 1987 Direct numerical simulation of plane Couette flow at a transitional Reynolds number. *JSME Intl J.* **30**, 57.

MOIN, P. & KIM, J. 1982 Numerical investigation of turbulent channel flow. *J. Fluid Mech.* **118**, 341.

NAGATA, M. 1990 Three-dimensional finite-amplitude solutions in plane Couette flow: bifurcation from infinity. *J. Fluid Mech.* **217**, 519.

NISHINO, K. & KASAGI, N. 1991 The structure of turbulence in a simulated plane Couette flow. *8th Symposium on Turbulent Shear Flows, Munich*, paper 28-3.

PAPAVASSILIOU, D. V. & HANRATTY, T. J. 1994 Secondary flow and residual turbulence in plane Couette flow. Submitted to *Phys. Fluids*.

REICHARDT, H. 1956 Über die Geschwindigkeitsverteilung in einer geradlinigen turbulenten Couettestömung. *Z. Angew. Math. Mech.* **36**, 26.

REICHARDT, H. 1959 Gesetzmässigkeiten der geradlinigen turbulenten Couettestömung. *Mitt. Max-Planck-Institut für Strömungsforschung*, no. 22. Göttingen.

ROBERTSON, J. M. 1959 On turbulent plane-Couette flow. *Proc. 6th Midwestern Conf. on Fluid Mech.* University of Texas, Austin, p. 169.

ROBERTSON, J. M. & JOHNSON, H. F. 1970 Turbulence structure in plane Couette flow. *J. Engng Mech. Div. ASCE* **96**, 1171.

ROBINSON, S. 1991 Coherent motions in the turbulent boundary layer. *Ann. Rev. Fluid Mech.* **23**, 601.

SCHEWE, G. 1983 On the structure and resolution of wall-pressure fluctuations associated with turbulent boundary layer flow. *J. Fluid Mech.* **187**, 61.

SHAH, D. A. & ANTONIA, R. A. 1989 Scaling of the "bursting" period in turbulent boundary layer and duct flows. *Phys. Fluids* A **1**, 318.

TILLMARK, N. & ALFREDSSON, P. H. 1991 An experimental study of transition in plane Couette flow. In *Advances in Turbulence 3* (ed. A.V. Johansson & P.H. Alfredsson), p. 235. Springer.

TILLMARK, N. & ALFREDSSON, P. H. 1992 Experiments on transition in plane Couette flow. *J. Fluid Mech.* **235**, 89.

TILLMARK, N. & ALFREDSSON, P. H. 1993 Turbulence in plane Couette flow. *Appl. Sci. Res.* **51**, 237.

TILLMARK, N. & ALFREDSSON, P. H. 1994 Structures in turbulent plane Couette flow obtained from correlation measurements. *5th European Turbulence Conference, Siena*.

TOWNSEND, A. A. 1976 *The Structure of Turbulent Shear Flow*, 2nd edn. Cambridge University Press.